Tuning Work Function and Conductivity of Methylhydroxyl Functionalized PEDOT-MeOH:PSS as a Hole Transport Material for Perovskite Solar Cells

Hao Dong

A thesis
submitted in partial fulfillment of the
requirements for the degree of
Master of Science in Chemical Engineering

University of Washington
2019

Committee:
Qiuming Yu
Samson Jenekhe

Program Authorized to Offer Degree:
Chemical Engineering

University of Washington

Abstract

Tuning Work Function and Conductivity of Methylhydroxyl Functionalized PEDOT-MeOH:PSS as a Hole Transport Material for Perovskite Solar Cells

Hao Dong

Chair of the Supervisory Committee:
Professor Qiuming Yu
Department of Chemical Engineering

A hole transport material poly(hydroxymethylated-3,4-ethylenedioxythiophene):polystyrene sulfonate (PEDOT-MeOH:PSS) was synthesized using the oxidative chemical polymerization method and deployed in inverted p-i-n $MAPbI_3$ perovskite solar cells (PVSCs). By introducing a methylhydroxyl (-MeOH) function group to the oxyethylene ring of EDOT, it lowers the highest unoccupied molecular orbital of PEDOT-MeOH. In addition, the MeOH function group allows the formation of hydrogen bonds among EDOT-MeOH monomers and with sulfate groups on PSS, promoting the growth of long chain PEDOT-MeOH and enhancing the doping efficiency. The work function and conductivity of PEDOT-MeOH:PSS were tuned via varying the amount of PSS and ferric oxidizing agent used in the polymerization and further via adding ethylene glycol as the secondary doping. The optimized PEDOT-MeOH:PSS-based PVSCs overperformed the PEDOT-PSS-based PVSCs because of better aligned energy level and enhanced conductivity of PEDOT-MeOH:PSS. This work provides new insights on developing hole transport materials to enable efficient inverted p-i-n PVSCs.

Table of Contents

LIST OF FIGURES

ACKNOWLEDGEMENT

I want to express my deepest appreciation to my advisor Professor Qiuming Yu for her guidance, encouragement and help, my group members Monica Esopi, Gabriella Tosado, Erjin Zheng, Zhiyin Niu, Zonglun Li, Zizhao Xu, Shukun Zhong, Emerson Chen, Wenxin Cao, Jacob Albrikan, Yiyu Lin and Xiaoyu Zhang for their intelligent ideas and my parents for their unconditional support. I also want to thank Professor Samson Jenekhe specially for being the committee member.

Chapter 1. Introduction

In the past decade, perovskite solar cells (PVSCs) have experienced a rapid development and has been regarded as a fourth-generation photovoltaic technology[1, 2]. Recently, power conversion efficiency (PCE) of the single junction PVSCs has reached 23.7%[3], and PCE for the monolithic perovskite/silicon solar cells has reached 28%[4]. Compared with other types of photoactive materials, inorganic-organic hybrid perovskites have the advantages such as sharp absorption edge and large absorption coefficient[5], long charge carrier diffusion length (100-1000 nm)[6], high charge mobility ($> 7.5\ \mathrm{cm^2\ V^{-1}\ s^{-1}}$ for electrons and $> 12.5\ \mathrm{cm^2\ V^{-1}\ s^{-1}}$ for holes)[7], and tunable band gap[8].

PVSCs typically adopted three device configurations: mesoporous, conventional and inverted structures. The mesoporous and conventional structured PVSCs have the electron transport layer (ETL) and hole transport layer (HTL) placed at the bottom and top of the perovskite light absorption active layer, respectively, to form the n-i-p structure, while the inverted structured PVSCs have the HTL and ETL at the bottom and top of the perovskite layer, respectively, to form the p-i-n structure[9]. Although the high PCE records were achieved by the mesoporous and the conventional n-i-p structured PVSCs[3, 10-12], the inverted p-i-n structured PVSCs have attracted more attentions because of good solution processability and low-temperature (<150 ℃) solution fabrication processes, making them a great candidate for future commercialization[9]. poly(3,4-ethylenedioxythiophene):poly (styrenesulfonate) (PEDOT:PSS) has been used as the HTL in inverted structured PVCSs. As a benchmark hole transport material, PEDOT:PSS has the advantages such as solution processability, high transparency, and good flexibility[13]. However, PVSCs based on PEDOT:PSS usually have lower open-circuit voltage (V_{oc}) (0.88-0.95 V) than their counterparts (>1.05 V) with the conventional structure[14-16]. Moreover, relatively low conductivity[13], poor electron-blocking capacity[17], and low charge mobility[18] (~0.045 $cm^2 V^{-1} s^{-1}$) of PEDOT:PSS and low-quality crystallization of $MAPbI_3$ perovskite grown on PEDOT:PSS[19] are also detrimental to the operational parameters of PVSCs including V_{oc}, short-circuit current density (J_{sc}), and fill factor (FF). In principle, V_{oc} is mainly determined by the band gap (E_g) of perovskite and voltage losses. Band gap defines the upper limit of V_{oc} and is an intrinsic property of perovskite. According to Shockley−Queisser theory, voltage loss due to radiative recombination above the band gap is unavoidable, which is typically 0.25 to 0.30 eV for PVSCs[20]. Another type of voltage loss for PVSCs originates from nonradiative charge recombination that occurs both within the perovskite layer and at the interface between perovskite and HTL or ETL[21-23]. For PVSCs involving PEDOT:PSS HTL, voltage loss is mainly due to the mismatched energy level between the work function (4.9-5.2 eV) of PEDOT:PSS[24] and the valence band maximum (~ -5.4 eV) of $MAPbI_3$ perovskite[25]. The inferior electrical conductivity of the PEDOT:PSS layer also leads to high series resistance, which causes more energy loss within PEDOT:PSS HTL[26]. According to Shockley equation, J_{sc} can be influenced by the series resistance and shunt resistance of devices and temperature[27]. Therefore, a high series resistance can also lower J_{sc}[18, 26, 28]. Less hole transport efficiency, resulted from the low conductivity and low charge mobility of PEDOT:PSS, causes an unbalanced charge carrier transport, which creates charge carriers accumulation and induces smaller shunt resistances, resulting in a low FF in PVSCs[29].

In order to address these problems and improve the electronic properties and surface morphology of PEDOT:PSS, numerous efforts have been made to shed light on the polymerization process of PEDOT:PSS to tune the structure of PEDOT:PSS or to modify the polymer complex. As an insulating polyelectrolyte, PSS is used in the chemical polymerization to dope the positively charged conductive PEDOT backbone and to stabilize hydrophobic PEDOT in aqueous solution. Therefore, the molecular weight and polydispersion of PSS and the composition ratio between PSS and PEDOT that are used in chemical polymerization have influence on the work function, conductivity, crystallinity and morphology of PEDOT:PSS thin films[24, 30-32]. The work function tends to be strongly dependent on the amount of PSS at the film surface. Enriched PSS layer at the surface can raise the work function of PEDOT:PSS thin films, which can be achieved by adding high composition ratio of PSS to PEDOT, using low molecular weight PSS to allow PSS easily migrate to the surface, and replacing water with ethanol/water mixture as the medium to promote phase segregation[30, 32]. The conductivity is more related to the oxidative state and crystallinity of PEDOT as well as the complex structure of PEDOT:PSS that affect the charge carrier density and mobility. Narrower molecular weight distribution of PSS can enhance the crystallinity of PEDOT:PSS thin films and thus increase the conductivity[31]. Low molecular weight PSS may offer better chain mobility to allow a better connection between conducting PEDOT grains to form a better conducting pathway and thus increase the conductivity[30]. Increasing the composition ratio of PSS to PEODT leads to reduce the conductivity because of PSS shells block the conducting pathway[30, 32]. The phase segregation of PEDOT and PSS domains induced by adding ethanol to water in the reaction medium resulted in a slight increase of the conductivity compare to PEDOT:PSS synthesized with pure water[30].

Post-polymerization modifications have also been explored to further tune the electronic and surface properties of PEDOT:PSS thin films to improve the performance of PVSCs. A mild organic base imidazole was added into PEDOT:PSS emulsion to adjust the pH value of PEDOT:PSS, leading to the change of electronic properties and surface morphology. A basic state

PEDOT:PSS yielded a larger work function of 5.31 eV, which aligns better with the valence band maximum of $MAPbI_3$ perovskite, resulting in an obvious increase of V_{oc} from 0.88 V to 1.06 V and PCE from 12.7% to 15.7%, while no significant changes for J_{sc} and FF[33]. Mixing polymer poly(2-ethyl-2-oxazoline) (PEOz) with PEDOT:PSS emulsions yielded a deeper work function of 5.3 eV, larger perovskite grain sizes, reduced hysteresis, and longer life time. The average V_{oc}, J_{sc}, FF, and PCE of the $MAPbI_3$ devices with the PEOz-PEDOT:PSS HTL were enhanced from 0.92 V, 15.98 mA cm^{-2}, 0.75, and 11.03% to 1.06 V, 20.05 mA cm^{-2}, 0.78, and 16.58%, respectively, because the PEOz-PEODT:PSS HTL reduces the perovskite hole trap-state density and the noncapacitive current[34]. Mixing 0.5 vol% of polyethylene oxide (PEO) with PEDOT:PSS greatly increased the conductivity by almost three orders of magnitude and smoothed the PEDOT:PSS thin film surface, yielding enhanced J_{sc} and FF though similar V_{oc} for the $MAPbI_3$ PVSCs with PEO doped PEDOT:PSS HTL compared to those with the conventional PEDOT:PSS HTL[28]. $MAPbI_3$ PVSCs using PEDOT:PSS with 10 vol% dimethyl sulfoxide (DMSO) as the HTL exhibited an enhanced J_{sc} of 22.35 mA cm^{-2}, compared with 17.27 mA cm^{-2} for the device with the untreated PEDOT:PSS HTL, due to the improved conductivity of PEDOT:PSS. The boosted device performance also benefited from the enlarged perovskite grain sizes and suppressed interfacial recombination with the DMSO treated PEDOT:PSS HTL[35].

Copolymerization of 3,4-ethylenedioxythiophene (EDOT) with other monomers has also been applied to modify PEDOT:PSS. EDOT was copolymerized with dopamine (DA) to form P(EDOT-DA):PSS, which exhibits a large work function of 5.33 eV and reduced acidity. The V_{oc} of $MAPbI_{3-x}Cl_x$ PVSCs was increased to 1.08 V from 0.97 V, although the J_{sc} and FF were slightly decreased. The reduced acidity of P(EDOT-DA):PSS highly enhanced long-term device durability under unencapsulated condition[36]. The effects of DA in P(EDOT-DA):PSS HTL was further investigated for $FA_yMA_{1-y}PbI_xBr_{3-x}$ PVSCs[37]. Besides deeper work function, P(EDOT-DA):PSS offers a higher radical content and efficient passivation of the undercoordinated Pb atoms, by the amino and hydroxyl groups in DA, on the perovskite at the interface, which reduces charge-recombination rate and increases the charge-extraction efficiency. As a result, a high PCE of 18.5% was achieved because of the enhancement of all PV parameters. The better device stability in air was also demonstrated by using the P(EDOT-DA):PSS HTL[37]. To further increase the work function for the copolymerized DA and EDOT, a branched macromolecule, lignosulfonate (LS), was used to replace PSS. P(EDOT-DA):LS exhibited an enlarged work function of 5.45 eV, which leads to an increase of V_{oc} from 0.86 V for $MAPbI_3$ PVSCs based on PEDOT:PSS to 1.02 V for P(EDOT-DA):LS devices. Importantly, the reduced acidity to a pH value of 5.2-5.4 and hydrophobic networks of LS gave a better stability for the devices with P(EDOT-DA):LS HTLs[38].

In this work, we proposed a new strategy to modify the electronic, structural, and morphological properties of PEDOT:PSS by introducing a methylhydroxyl (-MeOH) function group to the oxyethylene ring of EDOT to obtain hydroxymethylated-3,4-ethylenedioxythiophene (EDOT-MeOH) monomers and to further polymerize them to water soluble poly(hydroxymethylated-3,4-ethylenedioxythiophene):polystyrene sulfonate (PEDOT-MeOH:PSS) (Fig. 1.1a) using the oxidative chemical polymerization method. Because of the electronegativity of -MeOH function group, it is expected that the highest unoccupied molecular orbital (HOMO) of PEDOT-MeOH could be lowered and thus increase the work function of PEDOT-MeOH:PSS. The -MeOH function group can form hydrogen bonds among EDOT-MeOH monomers and with sulfate groups on PSS, respectively, which could promote the formation of long chain PEDOT-MeOH and enhance doping efficiency because EDOT-MeOH monomers are in the vicinity of each other and with PSS chains during polymerization. As a result, it is expected that the conductivity of PEDOT-MeOH:PSS could be increased. We systematically varied the amount of ferric oxidizing agent in polymerization to control the reaction kinetics, the chain length, and the oxidation state of polymers. We also varied the amount of PSS used in polymerization to control the doping level and work function of synthesized PEDOT-MeOH:PSS. Furthermore, we added ethylene glycol (EG) in the synthesized PEDOT-MeOH:PSS to further tune their micro-structures and conductivities. With the increase of the amount of EG, Raman scattering vibrational spectroscopic results revealed that the population of the quinoid structure within the PEDOT-MeOH backbone was increased and atomic force microscope (AFM) images showed the surface morphology of PEDOT-MeOH:PSS thin films became smoother. The inverted structured $MAPbI_3$ PVSCs with PEDOT-MeOH:PSS treated with EG exhibited the enhanced V_{oc} and J_{sc} because of the enlarged work function and conductivity.

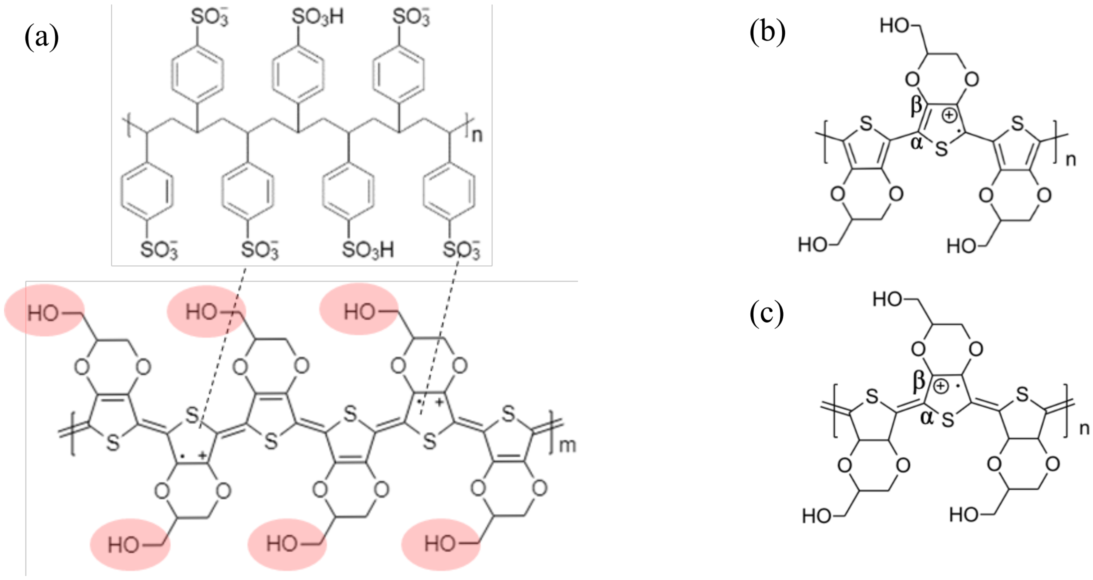

Figure 1.1 (a) Molecular structure of PEDOT-MeOH:PSS. (b) Benzoid and (c) quinoid structure of PEDOT-MeOH backbone.

Chapter 2. Experimental Method

2.1. Materials

3,4-dimethoxythiphene, 3-chloro-1,2-propanediol, p-toluene sulfonic acid monohydrate, toluene, hexane, CH_3COONa, dimethyl sulfoxide (DMSO), Na_2SO_4, sodium hydroxide (NaOH), Poly(4-styrenesulfonic acid) (PSSH, MW ~75,000 18 wt% in H_2O), sodium persulfate ($Na_2S_2O_8$), iron (III) sulfate hydrate ($Fe_2(SO_4)_3$), lead (II) iodide (PbI_2), and γ-butyrolactone (GBL) were purchased from Sigma-Aldrich, U.S.A. Methylene chloride (DCM, 99.9%), ethylene glycol (EG, 99.9%), and 2-propanol (IPA, 99.9%) were purchased from Fisher Chemical company. Ion exchangers (MP62 and S108H) were purchased from LANXESS Corporation. PEDOT:PSS (Al 4083) was purchased from Heraeus Company. Methylammonium iodide (MAI) was purchased from Greatcell Solar (Queanbeyan, Australia). $PC_{60}BM$ (> 99.5%) was purchased from American Dye Source (Quebec, Canada). All chemicals were used as received without any further purification.

2.2. Synthesis of EDOT-MeOH

3,4-dimethoxythiphene (5 g), 3-chloro-1,2-propanediol (12 g), p-toluene sulfonic acid monohydrate (0.676 g), and toluene (118 mL) were added into a three-neck flask. The system was purged with N_2 flow for 30 min and stirred vigorously at 95 °C under N_2 protection for 24 h. After removing of toluene under reduced pressure, the residue was purified by column chromatography (silica gel, hexane/methylene chloride = 8/2 v/v) to give 0.78 g 2-(chloromethyl)-2,3-dihydrothieno[3,4-b][1,4]dioxine (EDOT-MeCl).

To a round-bottom flask, EDOT-MeCl (0.5 g), CH_3COONa (0.365 g), and DMSO (7.869 mL) were added and the mixture was stirred at 120 ℃ for 2 h. The mixture was then poured into water and extracted with DCM. After extraction, Na_2SO_4 was added into DCM phase to dry the organic solution. Then the rotary evaporation was used to remove DCM and the achromatous oily liquid was obtained after rotary evaporation. The liquid was transferred into another clean round-bottom flask equipped with a reflux condenser. Then a solution of NaOH (0.367 g) in deionized (DI) water (10.5 mL) was added into the flask, and the system was refluxed at 105 ℃ for 1h. After the mixture was cooled down to the room temperature, DI water (5.8 mL) was added and the pH value was adjusted to 2. The acidified solution was extracted with DCM and after rotary evaporation, 0.45 g hydroxymethylated-3,4-ethylenedioxythiophene (EDOT-MeOH) was obtained. ^{1}H NMR results (400MHZ $CDCl_3$) of as-synthesized EDOT-MeOH is: δ 6.35 (s, 2H), δ 4.23 (d, 2H), δ 4.12 (m, 1H), 3.88 (m, 2H).

2.3. Synthesis of PEDOT-MeOH:PSS

The molar ratios of PSSH, $Na_2S_2O_8$, $Fe_2(SO_4)_3$, and NaOH to monomer EDOT-MeOH used in the synthesis are listed in Table 1. The amount of PSSH and $Fe_2(SO_4)_3$ were varied in the polymerization. We denoted the samples synthesized with the amount of PSSH that has the same molar ratio with PEDOT as the commercial Al 4083 (PSSH:PEDOT = 4.64:1, m:m) as PSS100-L or PSS100-H, where L and H represent the samples synthesized with low and high molar ratio of $Fe_2(SO_4)_3$ to EDOT-MeOH monomer, respectively. Samples synthesized with 80% and 60% of the original PSSH and high or low molar ratio of $Fe_2(SO_4)_3$ to EDOT-MeOH monomer were denoted as PSS80-H (L) and PSS60-H (L), respectively. Here, the synthesis of PSS100-L is used as an example to describe the procedure of polymerization. PSSH (2.505 mL) was dispersed in DI water (9 mL), poured into a conical flask that has EDOT-MeOH (0.1014 g), and stirred for 10 min to form an emulsion. To the emulsion, $Na_2S_2O_8$ (0.6267 g) dissolved in DI water (1 mL), $Fe_2(SO_4)_3$ (0.0118 g) dissolved in DI water (1 mL), and a half volume of NaOH (0.0547 g) dissolved in DI water (1 mL) were added. More DI water (3.7 mL) was used to wash the vials and then transferred into the emulsion. The light-yellow mixture turned to blue within 10 min after the $Na_2S_2O_8$, $Fe_2(SO_4)_3$, and NaOH solutions were added. The remaining half volume of NaOH solution was slowly added into the emulsion in 3 h using a syringe pump. Then after 24 h, the cation and anion exchangers (MP62 and S108H) were added into the emulsion, and the mixture was stirred for 2 h. The emulsion was filtered through the vacuum suction to remove the ion exchangers and then transferred into a clean vial. In order to collect ultraviolet-visible (UV-Vis) spectra, 100 μL PEDOT-MeOH:PSS emulsion was added into a clean vial and then 3.5 mL DI water was then added in the vial. After mixing by shaking, the mixture was transferred into a quartz cuvette via a syringe. The UV-Vis absorption spectra were collected using a Varian Cary 5000 UV-Vis-NIR spectrophotometer.

2.4. Modification of PEDOT-MeOH:PSS with Ethylene Glycol

The pristine PEDOT-MeOH:PSS polymers were treated with 2-6 vol% EG. To prepare PSS100-L with 2 vol% EG emulsion, to a clean vial, PSS100-L (294 mL) emulsion was added and then EG (6 mL) was added in to the emulsion. The mixture was stirred overnight and prepared for further use. Other pristine PEDOT-MeOH:PSS polymers treated with different volumetric percent of EG were prepared following the same method, but the volumes of PEDOT-MeOH:PSS and EG were changed accordingly.

2.5. Characterizations of PEDOT:PSS and PEDOT-MeOH:PSS Thin Films

Glass substrates were cut into 1.5 cm x 1.5 cm and cleaned in sequence in detergent in DI water, DI water, acetone, and IPA each for 15 min via ultrasonication. After being dried in oven, the substrates were treated in oxygen plasma cleaner for 10 min. PEDOT-MeOH:PSS or PEDOT:PSS emulsion filtered by nylon filters (0.45 μm) was spin-coated on the cleaned glass substrates at the speed of 3000 rpm for 60 s, followed by annealing at 120 °C for 25 min in air. The sheet resistance and thin film thickness were measured using the four-point probe measurement method (Bridge Company) and Olympus OLS4100 Optical Profilometer, respectively. Morphology of PEDOT-MeOH:PSS thin films was characterized with a tapping mode atomic force microscope (TM-AFM) using a Digital Multimode AFM equipped with a Nanoscope IVa controller. Raman Spectra of PEDOT-MeOH:PSS and PEDOT:PSS thin films were acquired using Thermo SCIENTIFIC DXR2 Raman Microscope. A 532 nm green laser with the power of 1 mW was focused on to the sample surface through a 50x (N.A. = 0.5) lens. The spectra were collected with 1 s exposure time and 30 accumulations. To measure the work function of PEDOT-MeOH:PSS with the cyclic voltammetry method using an EG&G Princeton Applied Research 273 Potentiostat & Galvanostat, the Pt wire (1 mm diameter, Sigma-Aldrich), casted with PEDOT-MeOH:PSS annealed at 120 °C for 25 min in air, was used as the working electrode and the work function was measured following the previous paper[39].

2.6 $MAPbI_3$ Perovskite Thin Films Formation and Characterization.

ITO coated glass substrates (10 ohm sq^{-1} ITO, Colorado Concept Coatings LLC) were cut into 1.5 cm x 1.5 cm and cleaned following the procedure described above. The filtered PEDOT-MeOH:PSS emulsion (0.45 μm nylon filter) was spin-coated on the cleaned substrates at 3000 rpm for 60 s, followed by annealing at 120 °C for 25 min in air. The substrates coated with PEDOT-MeOH:PSS were transferred into a N_2 glovebox. The $MAPbI_3$ precursor solution was prepared by adding 1 M MAI with 1 M PbI_2 in 700 μL GBL and 300 μL DMSO. The filtered $MAPbI_3$ precursor solution (0.45 μm PTFE filter) was then spin-coated onto the PEDOT-MeOH:PSS/ITO/glass substrate at the speed of 1000 rpm for 15 s and 4000 rpm for 45 s. After 30 s had passed in the second stage of spin coating, 500 μL dry toluene was dropped onto the rotating film. The as-prepared film was then annealed at 100 °C for 10 min. UV-Vis absorption spectra were collected using a Varian Cary 5000 UV-Vis-NIR spectrophotometer. Scanning electron microscopy (SEM) images were acquired using a FEI Sirion SEM operated at 15 kV to analyze the surface morphology of perovskite thin films. Two-dimensional X-ray diffraction (XRD) patterns were collected with a Bruker GADDS D8 Focus Powder Discover diffractometer using Cu Kα radiation ($\lambda = 1.5419$ Å) and the data were processed using the EVA package provided by Bruker Axs to investigate the crystalline structures of perovskite thin films.

2.7. Perovskite Photovoltaic Device Fabrication and Characterization

The devices have the structure of ITO/PEDOT-MeOH:PSS/$MAPbI_3$/$PC_{61}BM$/BCP/Ag. To the $MAPbI_3$ perovskite thin film prepared as described above, a 65 μL filtered 15 mg mL^{-1} $PC_{61}BM$ in chloroform solution (0.45 μm PTFE filter) was spin-coated onto the $MAPbI_3$ layer at the speed of 4000 rpm for 60 s, followed by spin coating a 70 μL filtered bathocuproine (BCP) solution (0.5 mg mL^{-1} in IPA) onto the $PC_{61}BM$ thin film at the speed of 4000 rpm for 60 s. Finally, a 150 nm thick top silver electrode was thermally evaporated under high vacuum ($< 2 \times 10^{-6}$ Torr) through a mask, resulting in sixteen devices on a chip with the device area of 3.14 mm^2.

The photocurrent density–voltage (J–V) characteristics were measured in a N_2 glovebox with a Keithley 2400 Source Meter and a Solar Light Co. Xenon lamp (16S-300 W) with an AM 1.5 filter. Before measurements, the light intensity was calibrated to 100 mW cm^{-2} using a standardized National Renewable Energy Laboratory calibrated silicon solar cell. The scan range is -0.5 V to 1.5 V and the scan rate is 100 mV/s.

Chapter 3. Results and discussion

3.1. PEDOT-MeOH Synthesis and Characterization

Properties such as conductivity, work function and surface morphology of HTL have a direct impact to solar cell performance. Tuning these properties for PEDOT:PSS by changing the chemical polymerization conditions has been reported in the previous studies[24, 31, 32, 40]. Here, we focused on the investigation of how the side function group -MeOH on PEDOT backbone affects the oxidative chemical polymerization and how the amount of PSS and ferric oxidizing agent used in the polymerization affects the electronic, structural, and morphological properties of PEDOT-MeOH:PSS.

EDOT-MeOH monomer was first synthesized and the purity was verified by NMR. The molar ratios of PSSH, Na_2SO_8, $Fe_2(SO_4)_3$, and NaOH to monomer EDOT-MeOH for different polymerization batches of PEDOT-MeOH:PSS are summarized in Table 1. Ferric sulfate ($Fe_2(SO_4)_3$), as the initiator and the first oxidizing agent, has a high oxidizability[24, 41]. We used a low, 0.5, and a high, 0.63, molar ratio of $Fe_2(SO_4)_3$/EDOT-MeOH in the reactions to study its effect on the final products. Sodium persulfate ($Na_2S_2O_8$), as the secondary oxidizing agent, has a moderate oxidizability[24, 41]. For all batches, we kept the same molar ratio of $Na_2S_2O_8$/EDOT-MeOH as 4.47, which is three times compared to that used in the synthesis of PEDOT:PSS[24]. We conducted the polymerization using the molar ratio of 1.49 for $Na_2S_2O_8$/EDOT-MeOH but no reaction occurred. We added NaOH in the reactions with a molar ratio of NaOH/PSSH to be 0.5. During the course of polymerization, the mixtures went through the distinct changes. An emulsion was formed when mixed PSSH and EDOT-MeOH monomer in DI water because PSSH has both hydrophobic backbone and hydrophilic sulfate acid side groups and EDOT-MeOH is hydrophobic.

EDOT-MeOH monomers either diffused into the hydrophobic core of PSSH or formed hydrogen bonds with sulfate acid in water. The emulsion of EDOT-MeOH and PSSH turned blue from yellow within 10 min after $Na_2S_2O_8$ and $Fe_2(SO_4)_3$ solution and the half volume of NaOH were added. By then, the remaining half volume of NaOH solution was slowly added into the emulsion in 3 h using a syringe pump. After stirring for 1-2 h since the beginning of reaction, the emulsion turned to darker blue and became more viscous to the point that stirring was difficult and some big particles were formed. More particles were observed for the batches with the high molar ratio of $Fe_2(SO_4)_3$/EDOT-MeOH. After stirring for 5-6 h, the particles gradually disappeared and the mixture turned to less viscous. Finally, after 24 h, the dark blue emulsion was obtained with a freshly cut grass smelling and no precipitates.

Table 1. The molar ratios of PSSH, Na_2SO_8, $Fe_2(SO_4)_3$, and NaOH to monomer EDOT-MeOH used for the synthesis of PEDOT-MeOH:PSS. Samples are presented by the amount of PSSH and $Fe_2(SO_4)_3$ used in the synthesis. PSS100 denotes the mass ratio of PSSH to PEDOT-MeOH 6:1, m/m, which is the same mass ratio of PSS to PEDOT for the commercial Al 4083. PSS80 and PSS60 represent the amount of PSSH as 80% and 60% of the original amount of PSSH used in the synthesis, respectively. The L and H denote the low and high amount of $Fe_2(SO_4)_3$ used in the synthesis, respectively.

Sample	PSSH/ EDOT-MeOH	NaS_2O_8/ EDOT-MeOH	$Fe_2(SO_4)_3$/ EDOT-MeOH	NaOH/ EDOT-MeOH
PSS100-L	4.64	4.47	0.05	2.32
PSS100-H	4.64	4.47	0.63	2.32
PSS80-L	3.71	4.47	0.05	1.86
PSS80-H	3.71	4.47	0.63	1.86
PSS60-L	2.78	4.47	0.05	1.39
PSS60-H	2.78	4.47	0.63	1.39

Based on the experimental observations and previous studies of the oxidative chemical polymerization of PEDOT:PSS[24, 30, 32], we proposed a possible polymerization mechanism for PEDOT-MeOH as shown in Fig. 3.1. Unlike EDOT monomers, EDOT-MeOH monomers can form hydrogen bonds with PSS and water as well as among monomers (Fig. 3.1I). Similar to the previous studies for PEDOT:PSS[41, 42], ferric sulfate ($Fe_2(SO_4)_3$) oxidized EDOT-MeOH monomer into a cation radical that dimerized and was stabilized by the removal of two protons. Dimers were further oxidized by Fe^{III} ions to form cation radicals, and short-chian polymers formed as a classical stepwise polymerization (Fig. 3.1II). The high oxidizability of ferric sulfate caused the polymerization to proceed quickly, thereby generating more short-chain polymers, or EDOT-

MeOH oligomers. Hydrogen bonding between EDOT-MeOH oligomer and PSS as well as among EDOT-MeOH oligomers caused the mixture viscosity increasing. In the meantime, EDOT-MeOH oligomers formed insoluble particles in water phase. Adding one order of magnitude higher $Fe_2(SO_4)_3$ to the reaction mixture greatly accelerated the initial oxidization of monomers, forming a relatively large number of EDOT-MeOH oligomers, therefore, more insoluble particles in water. Adding sodium persulfate together with ferric sulfate in the initial period allowed slow polymerization and promoted the growth of longer polymer chain[41]. The Fe^{III}/Fe^{II} couples catalyzed the decomposition of persulfate ions $S_2O_8^{2-}$ into persulfate radical ($S_2O_8^{-}\cdot$) and sulfate radical ($SO_4^{-}\cdot$) (Fig. 3.1), which oxidized EDOT-MeOH oligomers to form long-chain PEDOT-MeOH polymers (Fig. 3.1III) and oxidized PEDOT-MeOH backbones that were doped by PSS (Fig. 3.1IV). Adding NaOH in the initial period adjusted the pH value of the reaction mixture, reducing the reactivity of Fe^{III}/Fe^{II} [39]. Slowly adding the rest half volume of NaOH in the first 3 h made polymerization in a controllable way and deprotonated PSSH to better dope oxidized PEDOT-MeOH backbone. The hydrogen bonding dominated interaction between PEDOT-MeOH and PSS turned into a more electrostatic interaction, and a PEDOT-MeOH core-PSS shell structure was formed, which greatly reduced the viscosity of the mixture. The EDOT-MeOH oligomer large particles in water were gradually polymerized, oxidized and formed the core-shell structure. By the end of reaction, the mixture became a dark blue soluble emulsion.

We collected the UV-Vis absorption spectra of the mixtures during the course of the reactions. UV-Vis absorption spectroscopy has been commonly used to study the oxidation level of PEDOT:PSS in the redox reaction induced either by electrochemical method[24, 43] or by oxidizing and reducing agents[44]. The distinct absorption peaks correspond to the neutral and oxidized

PEDOT:PSS. The neutral PEDOT:PSS shows an absorption peak centered around 600 nm. In the first and second oxidation stages, polarons and bipolarons are formed, showing the absorption peaks centered around 800 nm and above 1200 nm, respectively[45-47]. Figure 3.2a and b show the UV-Vis absorption spectra of PSS80-H and PSS80-L collected at the early and late stages of the reactions and after ion exchange. Strong polaron, especially bipolaron, peaks are shown in the UV-Vis absorption spectra of PSS80-H and PSS80-L collected at 6 h and 3 h, respectively, indicating that oxidization occurred immediately once the short-chain PEDOT-MeOH were formed. The bipolaron peaks decreased slightly but the polaron peaks increased slightly when the reactions occurred over 20 h, which might be due to the growth of oxidized short-chain PEDOT-MeOH into long-chain PEDOT-MeOH. We also noticed that the bipolaron peak decreased obviously accompanied by the increase of the polaron peak after ion exchange for both PSS80-H and PSS80-L samples, indicating that some bipolarons were doped by bivalent sulfate ions[48]. The UV-Vis absorption spectra of all synthesized PEDOT-MeOH:PSS after ion exchange and Al 4083 PEDOT:PSS are shown in Fig. 3.2c. It can be seen obviously that the peak intensity ratios of bipolraon to polaron for PSS100(80, 60)-L samples are higher than those for PSS100(80, 60)-H samples, so does Al 4083 PEDOT:PSS. We calculated the ratio of the intensity at 1200 nm to the intensity at 800 nm. They are 1.51 versus 1.21, 1.50 versus 1.34, and 1.30 versus 1.16 for PSS100-L/H, PSS800-L/H, and PSS60-L/H, respectively. Using a high molar ratio of $Fe_2(SO_4)_3$/EDOT-MeOH resulted in more short-chain PEDOT-MeOH formed in the early stage compared to using a low molar ratio of $Fe_2(SO_4)_3$/EDOT-MeOH. In the meantime, more persulfate radicals ($S_2O_8^- \cdot$) and sulfate radicals ($SO_4^- \cdot$) were formed, because of the high amount of Fe^{III}/Fe^{II} couples, promoting chain growth. Therefore, long-chain, less bipolraon PEDOT-MeOH polymers were formed in the batches using a high molar ratio of $Fe_2(SO_4)_3$/EDOT-MeOH, while short-chain, more polaron PEDOT-MeOH polymers were formed in the batches using a low molar ratio of $Fe_2(SO_4)_3$/EDOT-MeOH. The intrinsic differences of these synthesized PEDOT-MeOH polymers have a significant impact on the electronic, structural, and morphological properties of pristine and ethylene glycol treated PEDOT-MeOH:PSS thin films.

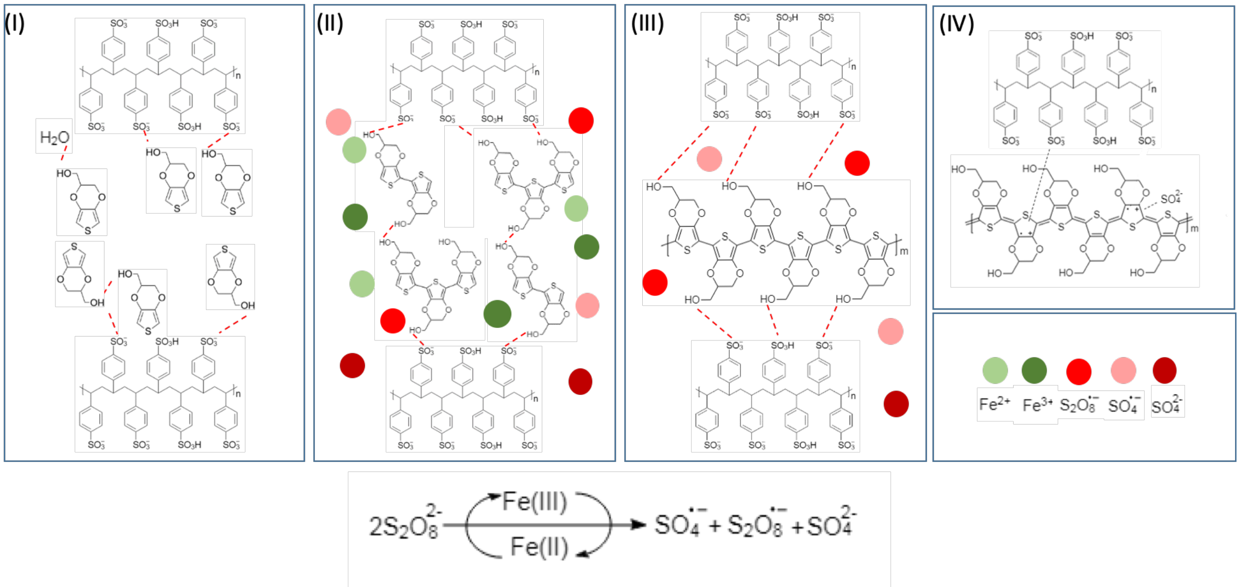

Figure 3.1 Schematic description of the possible oxidative chemical polymerization stages of EDOT-MeOH into PEDOT-MeOH, oxidized PEDOT-MeOH, and doped by PSS.

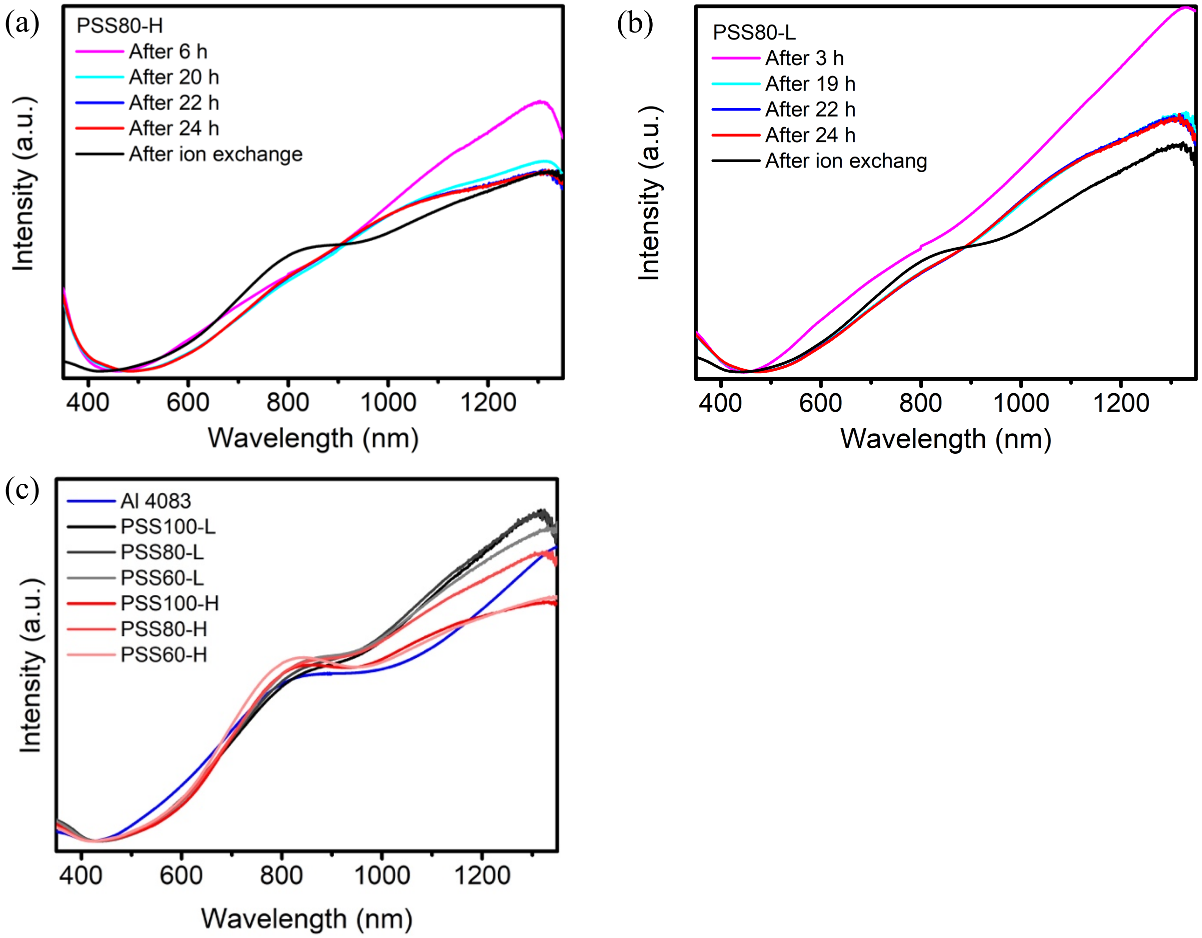

Figure 3.2 Time-span UV-Vis Spectra of (a) PSS80-H and (b) PSS80-L emulsions. (c) UV-Vis spectra of pristine PEDOT-MeOH:PSS emulsions after ion exchange and the commercial Al 4083 PEDOT:PSS. The UV-Vis spectra were normalized at the lowest points of Raman scattering intensity.

3.2. Conductivity and Work Function of Pristine PEDOT-MeOH:PSS

We measured the conductivity of the pristine PEDOT-MeOH:PSS thin films using four-point probe method, which are shown in Fig. 3.3a. Basically, electrical conductivity is the product of carrier charge (*e*), carrier concentration (*n*) (cm^{-3}) and carrier mobility μ ($cm^2\ V^{-1}\ s^{-1}$), expressed as $\sigma = ne\mu$, where e is a constant, n and μ can be modified via varying polymerization conditions. As a π-conjugated polymer, the carrier concentration and carrier mobility are highly determined by the PEDOT-MeOH backbone oxidative state, the chain-length, and the coplane and packing of backbone. PSS is an insulator, but it is also a dopant for oxidized PEDOT-MeOH. PSS is soluble in water, but it also has a hydrophobic backbone. Therefore, the conductivity of PEDOT-MeOH:PSS is also determined by the amount of PSS used in the synthesis and the microstructure of PEDOT-MeOH:PSS polymer complex. PSS100-H and PSS100-L PEDOT-MeOH:PSS polymers were polymerized with the molar ratio of EDOT-MeOH/PSS of 1:4.64 that is the same for the commercial Al 4083 PEDOT:PSS. While the conductivity of PSS100-L (0.034 S/m) is similar to that of the commercial Al 4083 PEDOT:PSS (0.030 S/m), the conductivity of PSS100-H (0.041 S/m) is higher. This could be due to the longer chain and more oxidized PEODT-MeOH formed by using one order of magnitude higher amount of $Fe_2(SO_4)_3$[24, 41, 42, 48]. In addition, the hydrogen bonding between EDOT-MeOH monomers and between EDOT-MeOH and PSS could facilitate the polymerization of PEDOT-MeOH chain and the doping of the oxidized PEDOT-MeOH as illustrated in Fig. 3.1. Longer PEDOT-MeOH chains at high doping level has more charge carriers and thus improve the conductivity of the PSS100-H PEDOT-MeOH:PSS as previously observed for PEDOT:PSS[24, 49]. Longer chain leads to a better conductivity has also been reported for other conjugated conducting polymers[50]. With the decrease of PSS to 80% and 60% of the original amount, the conductivity of PSS80-L and PSS60-L increases slightly to 0.035 and 0.041 S/m, respectively, while both PSS80-H and PSS60-H exhibit a larger increase to 0.054 and 0.059 S/m, respectively, which follows the same trend reported for PEDOT:PSS[30, 32]. The different impact on the increase of conductivity for the PEDOT-MeOH:PSS polymerized with high or low amount of $Fe_2(SO_4)_3$ could also be attributed to the different length and oxidative state of PEDOT-MeOH chains[41].

We measured the work function of pristine PEDOT-MeOH:PSS using the cyclic voltammetry (CV) method. The results are shown in Fig. 3.3b and the cyclic voltammograms are provided in Fig. 3.4. All pristine PEDOT-MeOH:PSS exhibited work functions greater than 5.2 eV, which are higher than the reported work function of PEDOT:PSS that is in the range of 4.9-5.2 eV[24, 51]. The high electronegativity of the methylhydroxyl groups[52] on the oxyethylene rings of PEDOT attracts the electron cloud on the thiophene conjugated plane, down-shifting the highest occupied molecular orbital (HOMO) level[53] and making thiophene rings more stable and harder to be oxidized. Hence, the work function of PEDOT-MeOH:PSS becomes larger, or the HOMO of PEDOT-MeOH:PSS becomes deeper. The amount of PSS and ferric oxidizing agent used in the polymerization has a remarkable impact on the work function of pristine PEDOT-MeOH:PSS. The work function of pristine PEDOT-MeOH:PSS increased with the increase of PSS regardless of low or high amount of ferric oxidizing agent was used (Fig. 2b). This trend is consistent with the previous studies for PEDOT:PSS[30]. More insulating PSS could protect PEDOT-MeOH conjugated polymers from oxidation, resulting in higher work function. For the PEDOT-MeOH:PSS having the same amount of PSS, using a high amount of ferric oxidizing agent led to a higher work function. The increased work function could be related to the longer PEDOT-MeOH chains yielded by the high amount of $Fe_2(SO_4)_3$ used in the polymerization. Longer PEDOT-MeOH chains tend to form a coil conformation within PSS shells, which could more effectively protect PEDOT-MeOH from oxidation. Our results clearly show that the work function of PEDOT-MeOH:PSS can be tuned by introducing an electrophilic function group on the PEDOT backbone, or by using different amount of PSS and ferric oxidizing agent in polymerization.

3.3. Chemical Structure and Surface Morphology of Pristine PEDOT-MeOH:PSS

In order to understand the effects of PSS and ferric oxidizing agent on the conductivity and work function from the molecular structure of pristine PEDOT-MeOH:PSS, we conducted Raman spectroscopic measurements on PEDOT-MeOH:PSS thin films. Raman scattering, complementary to infrared absorption spectroscopy, allows one to study the normal vibration modes and, subsequently, the structure of molecules. Moreover, it is reported that Raman spectroscopy is a very useful tool for studying the doping process in conjugated polymers[54-56]. During doping, the changes in the Raman spectra are interpreted in terms of modification of electronic distribution along the chain from the neutral structure with more evenly distributed electrons among thiophene rings to the quinoid structure dominated polaron oxidation state and further to the benzoid structure dominated bipolaron oxidation state. Figure 2c shows the Raman spectra of PEDOT-MeOH:PSS and Al 4083 PEDOT:PSS recorded in the range of 400-3400 cm^{-1}. The vibrational peaks at 991, 1110, and 1255 cm^{-1}, which are strong in PEDOT:PSS, are attributed to oxyethylene ring deformation, C-O-C deformation, and C_α-$C_{\alpha'}$ inter-ring stretching mode, respectively[54]. These peaks are weaker for PEDOT-MeOH:PSS samples because the adding of -MeOH side function group on oxyethylene ring pulls electron from oxyethylene ring, and thus affecting the vibrational modes. Peaks in the spectral window of 1300-1700 cm^{-1} are mainly due to the C_α-C_β symmetric and asymmetric vibrational modes. The significance of these vibrations is that the changes in the positions and intensities of the associated Raman bands are directly related to the doping[54-56], which are related to the oxidative chemical polymerization conditions. We deconvoluted the Raman spectra of all pristine PEDOT-MeOH:PSS and Al 4083 PEDOT:PSS in this range, which are shown in Fig. 3.5 and the peak positions are summarized in Table 3. Because of the co-existence of benzoid and qunoid structures in PEDOT-MeOH backbone, the same vibrational mode can be deconvoluted into two peaks corresponding to each type of the structure. The peaks also shifted slightly for different samples because of different reaction conditions. The deconvoluted Raman spectrum of PSS100-L is shown in Fig. 3.3d as an example. The deconvoluted peaks around 1350 cm^{-1} and 1382 cm^{-1} are attributed to C_β-C_β stretching vibration of benzoid and quinoid structure, respectively, showing that the quinoid peak is much stronger. These peaks are redshifted compared to the peaks at 1332 cm^{-1} and 1371 cm^{-1} for PEDOT:PSS, which is again due to the adding of MeOH side group on oxyethylene ring. The strong peak centered around 1440 cm^{-1} is due to the C_α=C_β symmetric stretching, which can be deconvoluted into two peaks at 1422 and 1445 cm^{-1}, corresponding to the benzoid and quinoid structure, respectively. It is reported that the C_α=C_β symmetric stretching band at 1414 cm^{-1} is mostly due to the vibration of the neutral structure. This peak shifts to around 1445 cm^{-1} when the portion of the oxidized PEDOT structure is increased[54, 55]. All pristine PEDOT-MeOH:PSS thin films show the C_α=C_β symmetric stretching band around 1445 cm^{-1}, indicating that all PEDOT-MeOH:PSS polymers are oxidized. Three peaks at 1504, 1544, and 1566 cm^{-1} correspond to the C_α=C_β asymmetric stretching vibration of the benzoid structure, the splitting of the C_α=C_β asymmetric stretching vibrations, and the C_α=C_β asymmetric stretching vibration of the quinoid structure, respectively[55, 56]. We determined the ratio of quinoid and benzoid structures in the synthesized PEDOT-MEOPH:PSS by calculating the peak area ratio of the bands corresponding to the quinoid and benzoid structure related to the C_α=C_β symmetric stretching, which are marked in red and green shadows in Fig. 3.3d, respectively. The peak area ratios for all pristine PEDOT-MEOH:PSS are plotted in Fig. 3.3a. For fixed PSS, the ratio of quinoid to benzoid structure decreases with the increasing amount of ferric oxidizing agent. However, this ratio increases with the increasing amount of PSS for the fixed amount of ferric oxidizing agent. The quinoid structure, corresponding to the polaron oxidation state, is known to be more rigid and form a linear conformation along PSS chains, while benzoid structure, corresponding to the bipolaron oxidation state, is more flexible and forms a coil conformation within PSS shells[24, 43, 57]. The higher amount of ferric oxidizing agent tends to create longer PEDOT chains, oxidize PEDOT to bipolaron dominated benzoid structure, and thereby form a coil conformation[24]. We speculate that the high amount of ferric oxidizing agent used in the reaction results in longer and more oxidized PEDOT-MeOH chains, which are flexible, and thus favor to benzoid structure. Increasing the amount of PSS can help longer chain PEDOT-MeOH interact more with PSS to form linear or expanded-coil conformation and thus quinoid structure to be more favorable[31].

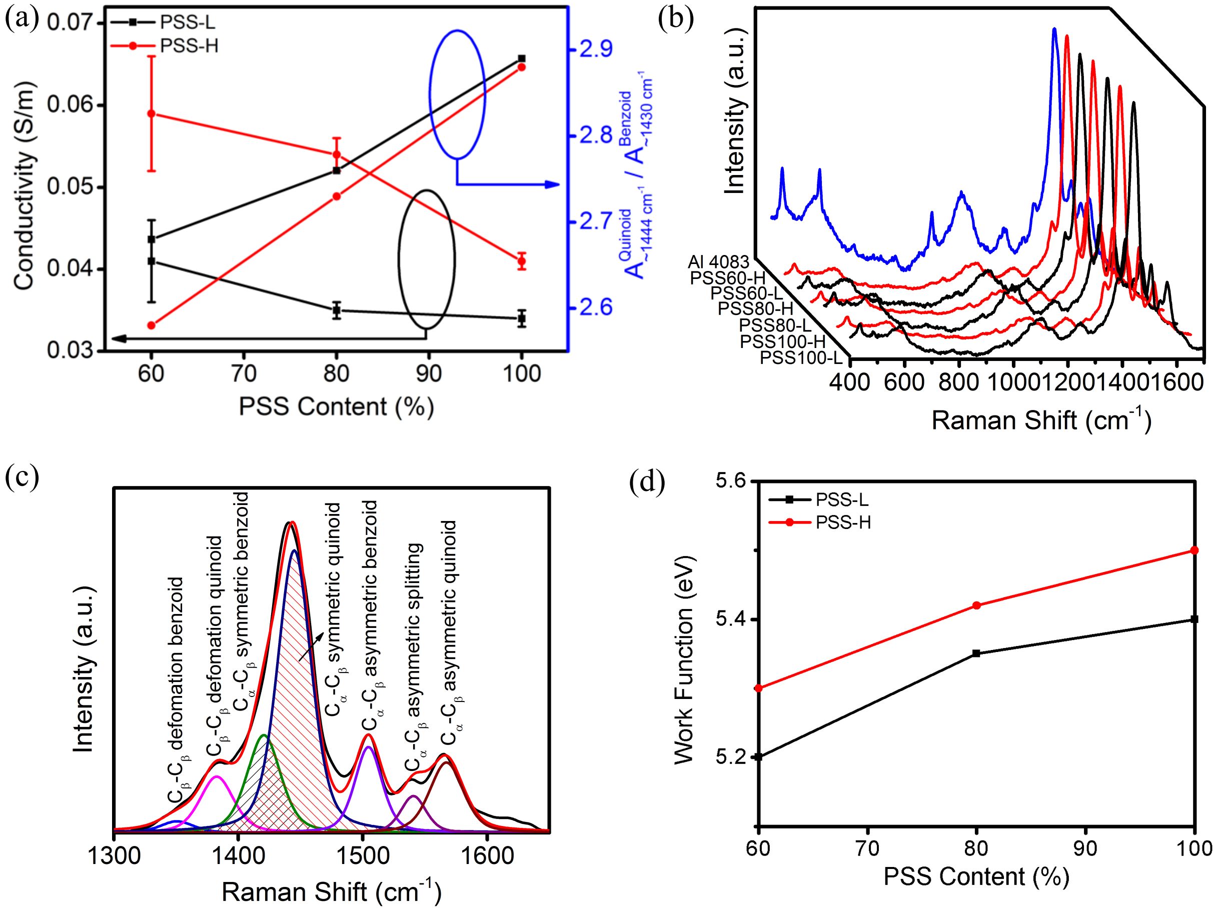

Figure 3.2 (a) Conductivity and the ratio of quinoid to benzoid structure of pristine PEDOT-MeOH:PSS thin films. (b) Work function of pristine PEDOT-MeOH:PSS measured with cyclic voltammetry. (c) Raman Spectra of pristine PEDOT-MeOH:PSS and Al 4083 PEDOT:PSS thin films. (d) Deconvoluted Raman spectrum of PSS100-L thin film with the C_α-C_β symmetric vibrational peaks corresponding to the benzoid and quinoid PEDOT-MeOH structures shadowed.

Table 2. Conductivity of commercial Al 4083 PEDOT:PSS and synthesized PEDOT-MeOH:PSS.

Sample	Resistivity (Ω/sq)	Thickness (nm)	Conductivity (S/m)
Al 4083	38.16±6.35	53.3±0.8	0.030±0.004
PSS100-L	29.80±0.26	41.2±0.4	0.034±0.001
PSS80-L	28.77±0.94	40.1±1.3	0.035±0.001
PSS60-L	24.45±3.32	32.6±4.3	0.041±0.005
PSS100-H	24.23±0.25	33.5±0.4	0.041±0.001
PSS80-H	18.49±0.39	25.3±0.5	0.054±0.002
PSS60-H	16.87±2.31	23.0±3.1	0.059±0.007

Table 3. Raman peak positions of the commercial Al 4083 PEDOT:PSS and PEDOT-MeOH:PSS with or without EG HTL.

HTL	EG Content (vol%)	C_β-C_β stretching benzoid	C_β-C_β stretching quinoid	C_α-C_β symmetric stretching benzoid	C_α-C_β symmetric stretching quinoid	C_α-C_β asymmetric stretching benzoid	C_α-C_β asymmetric splitting	C_α-C_β asymmetric quinoid
Al 4083	\	1332	1371	1417	1445	1499	1537	1570
PSS100-L	\	1351	1383	1421	1445	1502	1541	1568
PSS100-H	\	1351	1383	1421	1445	1502	1541	1568
	2	1353	1383	1424	1444	1508	1541	1567
	3	1351	1382	1424	1442	1508	1548	1564
	5	1351	1385	1429	1449	1505	1539	1567
PSS80-L	\	1352	1386	1428	1449	1504	1539	1565
PSS80-H	\	1354	1384	1426	1446	1505	1539	1566
	2	1352	1382	1424	1444	1508	1549	1564
	3	1352	1382	1424	1444	1508	1549	1564
	5	1352	1382	1424	1444	1508	1549	1564
	6	1355	1385	1427	1447	1508	1549	1564
PSS60-L	\	1355	1385	1426	1446	1508	1549	1564
PSS60-H	\	1352	1382	1424	1444	1508	1549	1564
	2	1352	1382	1424	1444	1508	1549	1564
	3	1355	1385	1427	1447	1507	1549	1564
	5	1355	1385	1427	1447	1508	1549	1564

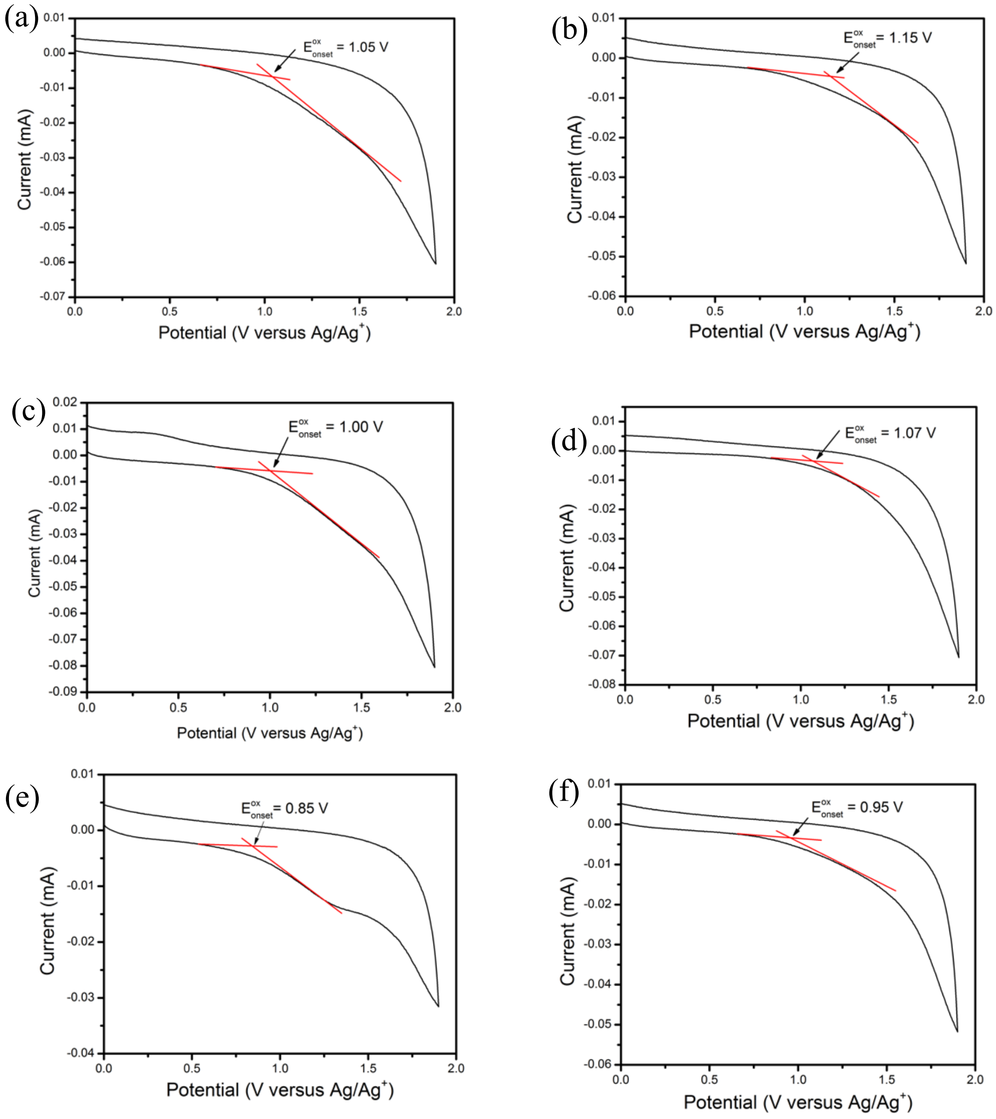

Figure 3.3 Cyclic voltammagram of (a) PSS100-L, (b) PSS100-H, (c) PSS80-L, (d) PSS80-H, (e) PSS60-L and (f) PSS60-H. During the experiment, the potential values were obtained in reference to the Ag/Ag+ electrode and were then converted in reference to the internal standard of ferrocenium/ferrocene (Fc+/Fc). Next, the potential values referenced to the Fc+/Fc redox couple were converted to reference a saturated calomel electrode (SCE) and used along with empirical correlations to estimate the work function of PEDOT-MeOH:PSS samples[39].

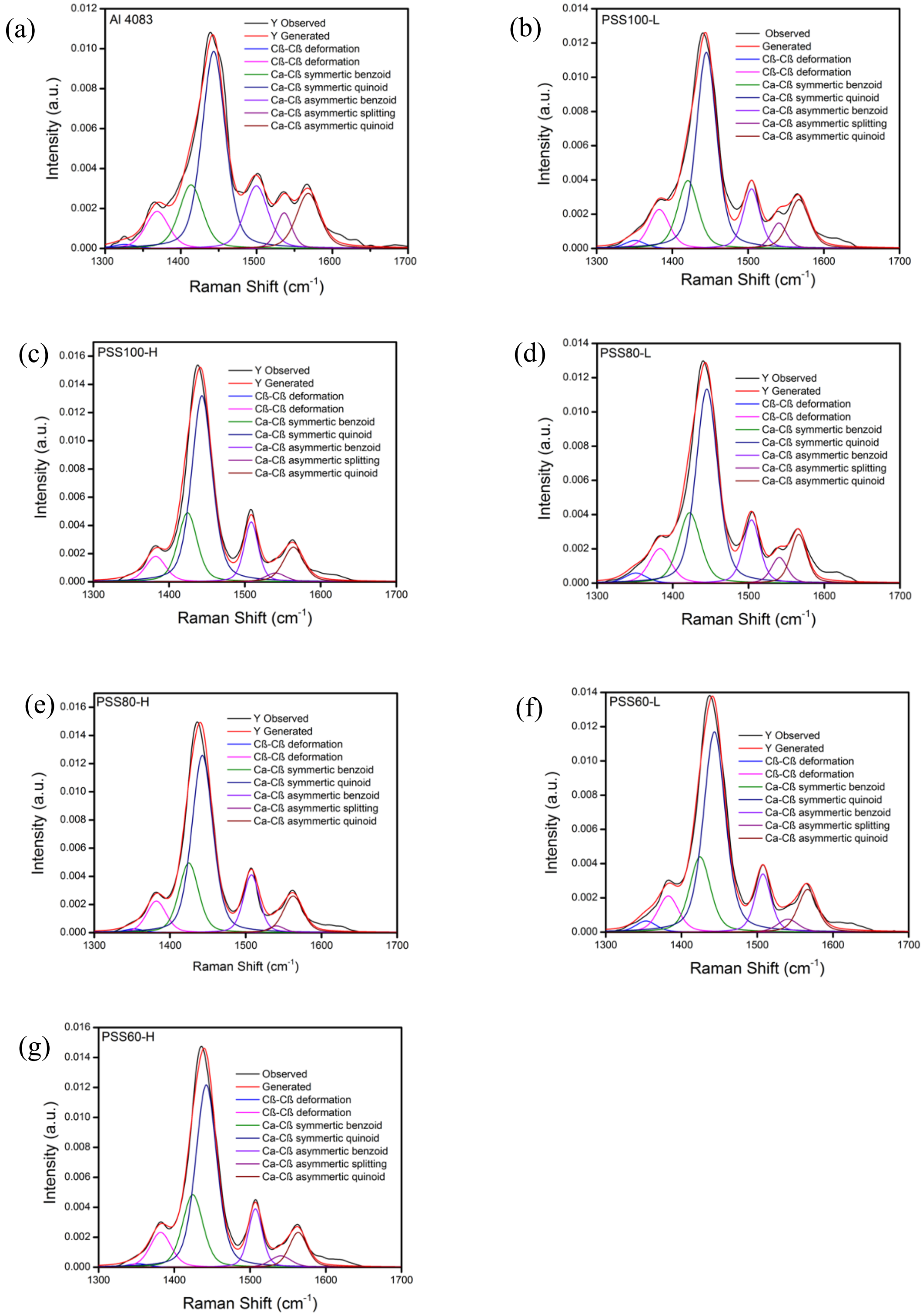

Figure 3.4 Peak fitting diagrams of (a) Al 4083, (b) PSS100-L, (c) PSS100-H, (d) PSS80-L, (e) PSS80-H, (f) PSS60-L and (g) PSS60-H.

Since the surface morphology of an HTL has a significant impact to charge transport and recombination at the interface of HTL and active layer, we measured the surface morphology of pristine PEDOT-MeOH:PSS using atomic force microscope (AFM). Large area (10 × 10 μm^2) topographic AFM images (Fig. 3.6) show that PEDOT-MeOH:PSS thin film surfaces exhibit smoother background compared to Al 4083 PEDOT:PSS but some particles are on the surfaces, especially for the PEDOT-MeOH:PSS polymerized with the high amount of ferric oxidizing agent. This is concurrent with more particles observed during the reactions. Smaller area AFM images (1 × 1 μm^2) in Fig. 3.7 show that all pristine PEDOT-MeOH:PSS films exhibit much smoother surfaces than that of Al 4083 PEDOT:PSS. The smoother surface could be the beneficial of hydrogen bonding in the early stage of polymerization, suppressing the phase segregation of hydrophobic PEDOT-MeOH and hydrophilic PSS domains. Reducing the amount of PSS has no significant impact to the surface morphology of pristine PEDOT-MeOH:PSS films but smoother, more uniform surfaces are shown for PEDOT-MeOH:PSS synthesized with the larger amount of ferric oxidizing agent used in the polymerization reaction. This is probably because longer PEDOT-MeOH chains can interact strongly with PSS, suppressing phase segregation.

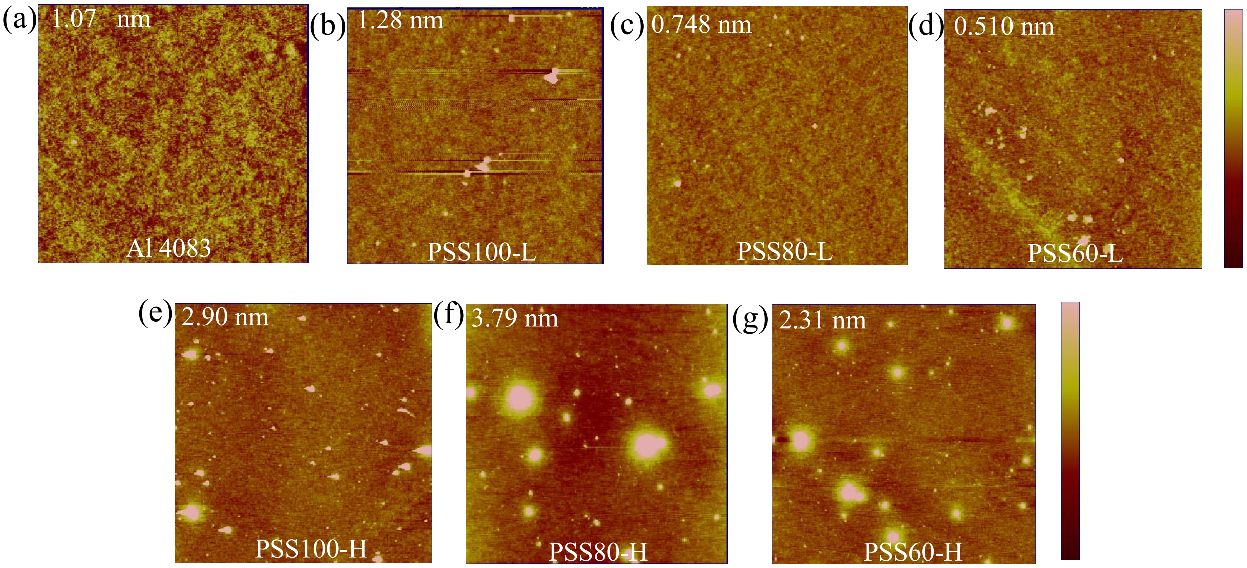

Figure 3.5 Large area (10 × 10 μm²) AFM images of (a) Al 4083, (b) PSS100-L, (c) PSS80-L, (d) PSS60-L, (e) PSS100-H, (f) PSS80-H, and (g) PSS60-H. The Z scale is 10 nm. The root mean square (RMS) roughness of each surface is shown in the images.

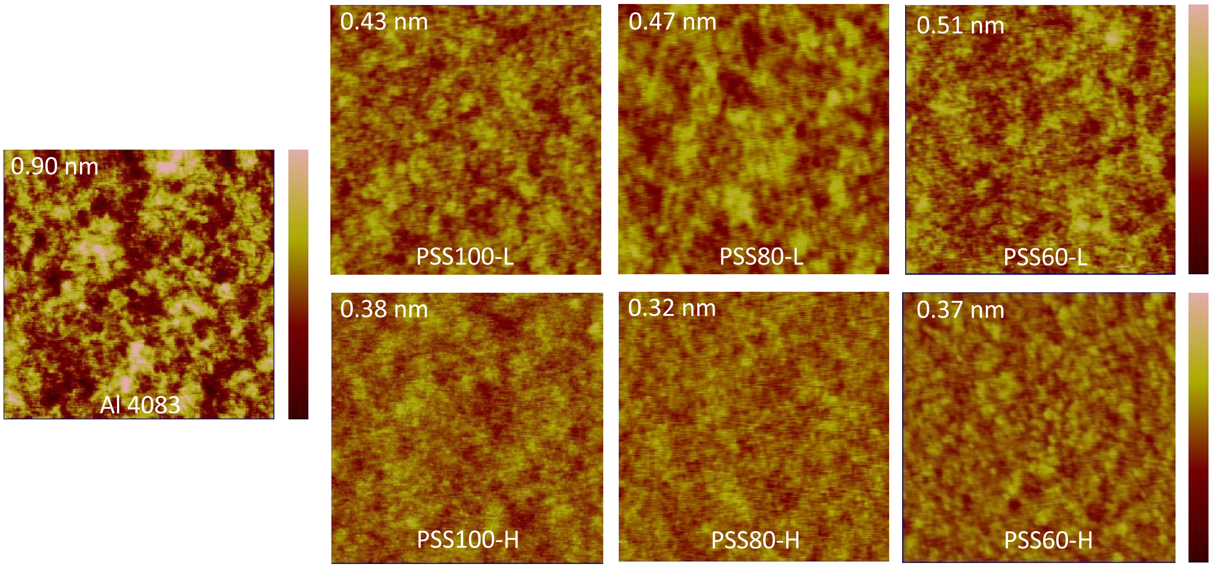

Figure 3.6 AFM topographic images (1 μm x 1 μm) of commercial Al 4083 PEDOT:PSS and the as-synthesized PEDOT-MeOH:PSS thin films. The z-scale bar is 5 nm for all images. The root mean square (RMS) roughness of the surface shown on top left corner of the corresponding image.

3.4. MAPbI3 PVSCs with HTLs Using Pristine PEDOT-MEOH:PSS and PEDOT:PSS

We grew $MAPbI_3$ perovskite thin films on pristine PEDOT-MeOH:PSS thin films using one-step anti-solvent washing solution process and fabricated solar cells with the structure of ITO/PEDOT-MeOH:PSS/$MAPbI_3$/$PC_{61}BM$/BCP/Ag to study the impacts of the electronic and surface morphological properties of PEDOT-MeOH:PSS on $MAPbI_3$ PVSCs. The top and cross-section SEM images of $MAPbI_3$ on PSS80-H PEDOT-MeOH:PSS show densely packed, pinhole-free perovskite thin film with grain size about ~100 nm (Fig. 3.8a). The x-ray diffraction (XRD) pattern (Fig. 3.8b) shows intense diffraction peaks at 14.0°, 28.3°, 31.8° and 35.0°, corresponding to the diffraction of (110), (220), (310) and (312) planes of tetragonal $MAPbI_3$, respectively. Small amount of PbI_2 presents in the perovskite film indicating by the tiny peak at 12.7°. The UV-Vis spectrum (Fig. 3.8c) shows a cut-off at 800 nm corresponding to the band gap of 1.55 eV.

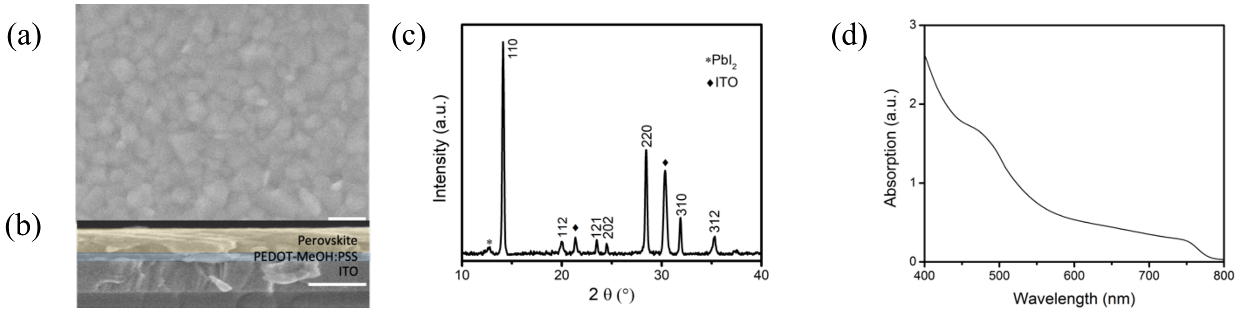

Figure 3.7 (a) Top and (b) cross-section SEM images, (c) XRD pattern, and (d) UV-Vis absorption spectrum of $MAPbI_3$ perovskite thin film fabricated on PSS80-H PEDOT-MeOH:PSS thin film spun on an ITO/glass substrate. The scale bar is 200 nm. The peaks located at 21.5° and 30.3° are attributed to the ITO. (c) XRD pattern of the $MAPbI_3$ perovskite thin film deposited on PSS80-H on an ITO substrate. (d) UV-Vis absorption spectrum of $MAPbI_3$ perovskite thin film fabricated on PSS80-H PEDOT-MeOH:PSS.

Figure 3.9 and Table 4 show the device performance statistics for the solar cells based on the pristine PEDOT-MeOH:PSS and PEDOT:PSS HTLs. The highest average PCE of 9.06% was achieved by the devices based on pristine Al 4083 PEDOT:PSS, while the average PCEs of the devices based on pristine PEDOT-MeOH:PSS showed different trends with PSS for PEDOT-MeOH:PSS polymerized with high or low amount of ferric oxidizing agent.

For the devices based on PSS100(80, 60)-L, the average PCEs were 7.68%, 5.92% and 3.47%, respectively, mainly due to the same decreasing trend for V_{oc} and J_{sc}. The decrease of V_{oc} of the devices with the HTL that has a reduced amount of PSS is closely related to the decrease of work function from 5.35 eV for PSS100-L to 5.32 eV for PSS80-L to 5.20 eV for PSS60-L, which is away from the better energy alignment with the valence band maximum (-5.4 eV) of $MAPbI_3$. The decrease of J_{sc} of the devices shows a contrary trend with the conductivity change versus PSS amount of these HTLs (Fig. 3.3b), indicating that the effect of low charge transport efficiency due to energy level mismatch suppresses the effect of slightly increased conductivity. The devices based on PSS80-L HTL exhibited the best average FF, which could be due to the better energy alignment and improved the conductivity of PSS80-L HTL.

For the devices based on PSS100(80, 60)-H, the average PCEs were 1.23%, 7.66% and 6.24%, respectively. The extremely low PCE of the devices based on PSS100-H PEDOT-MeOH:PSS HTL may result from the high work function (5.5 eV) of PSS100-H, which blocks hole transport from the valence band of $MAPbI_3$ that has the band edge energy of -5.4 eV. The unfavorable energy alignment is reflected by the very fluctuated V_{oc}, and extremely low J_{sc} and FF. The J_{sc}'s showed a linear increase, the same trend as the conductivity, with the reduced amount of PSS for

PSS100(80, 60)-H. The average J_{sc}'s were 13.30 and 16.76 mA cm^{-2} for the devices based on PSS80-H and PSS60-H HTLs, compared to 11.69 mA cm^{-2} for the devices based on PEDIT:PSS. Despite that J_{sc}'s were significantly increased, the V_{oc}'s and FF's, particularly FF's, of the devices based on PSS80-H and PSS60-H were decreased, leading to inferior PCE's compared to the devices based on PEDOT:PSS. The lower FF's for the devices based on pristine PEDOT-MeOH:PSS pointed out that further post-synthesis treatment of PEDOT-MEOH:PSS is needed to improve the electronic and morphological properties of PEDOT-MeOH:PSS.

Table 4. Device performance summary of the devices based on a pristine commercial Al 4083 PEDOT:PSS or a pristine PEDOT-MeOH:PSS HTL.

HTL	Voc (V)	Jsc (mA/cm^2)	FF (%)	PCE (%)	PCE$_{\text{Max}}$ (%)
Al 4083	0.99±0.01	11.69±0.75	74.3±1.7	9.09±0.46	9.62
PSS100-L	1.06±0.01	12.44±0.49	58.4±2.1	7.68±0.34	8.09
PSS100-H	0.82±0.24	6.98±0.34	22.8±6.3	1.23±0.22	1.35
PSS80-L	0.98±0.02	10.06±0.26	60.7±2.2	5.92±0.34	6.35
PSS80-H	1.00±0.08	13.30±1.44	57.7±3.6	7.66±0.40	8.43
PSS60-L	0.92±0.01	7.13±0.58	53.2±1.6	3.47±0.24	3.90
PSS60-H	0.80±0.06	16.76±0.31	46.6±3.4	6.24±0.96	6.36

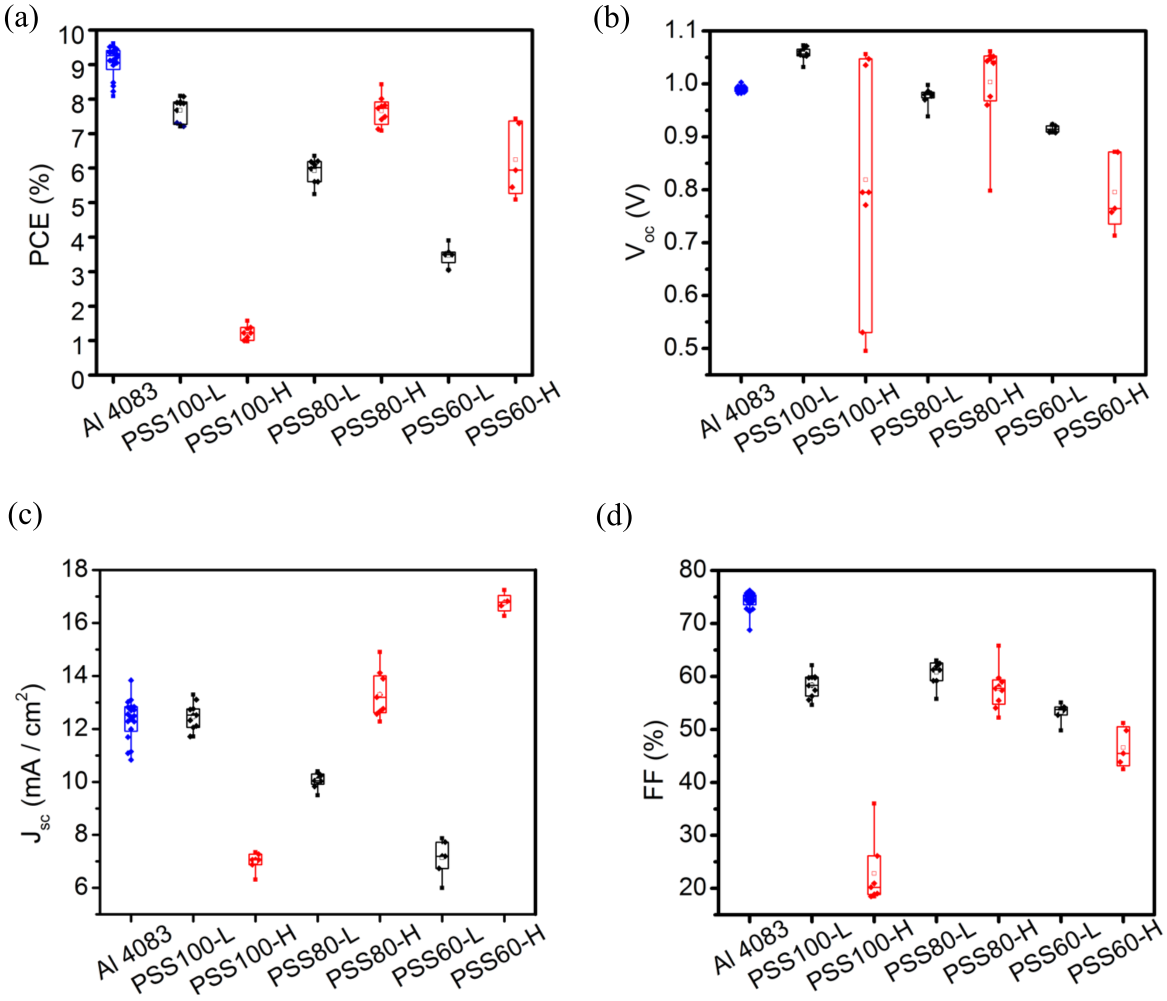

Figure 3.8 Statistics of (a) PCE, (b) Voc, (c) Jsc, and (d) FF of the solar cells with the device structure of ITO/HTL/MAPbI3/PC61BM/BCP/Ag and HTL of pristine Al 4083 PEDOT:PSS (blue), PSS100(80, 60)-L (black), and PSS100(80, 60)-H (red).

3.5. Ethylene Glycol Treatment for PEDOT-MeOH

Post-synthesis treatment of PEDOT:PSS has been widely used to tune the electronic, thermoelectronic, and morphological properties of PEDOT:PSS[33, 43, 57-60]. Sulfoxides, such as dimethyl sulfoxide (DMSO), and polyols, such as ethylene glycol (EG), are the most popular additives that have been used to increase the conductivity of PEDOT:POSS[57, 59, 60]. Structural change of the PEDOT backbone from benziod to quinoid and phase segregation of PEDOT and PSS domains are the two possible mechanisms for the conductivity enhancement of PEDOT:PSS treated with these additives. Structural change of PEDOT backbone from benzoid to quinoid makes more delocalized electron distribution on the PEDOT backbone. The linear quinoid structure may be more favorable after the addition of EG because EG promotes the change of PEDOT chains from the coil conformation into linear conformation[43, 59, 60]. Similar phenomenon was also reported using diethylene glycol (DEG) as the additive[61]. Phase segregation was also considered as an important factor in the enhancement of conductivity because the conductive PEDOT domains are able to segregate out from the insulating PSS shells with the aid of EG or DMSO to form better packed, crystalline PEDOT domains, which improves the charge transport efficiency[62-65]. Because of the hydroxyl group on PEDOT-MeOH, we expected that PEDOT-MeOH could have stronger interaction with EG via hydrogen bonding, facilitating the structural change of PEDOT-MeOH backbone from benzoid to quinoid as well as the phase segregation of PEDOT-MeOH domains from PSS domains, resulting in a significant improvement on conductivity.

We added 2, 3, and 5 vol% EG in pristine PEDOT-MEOH:PSS and Al 4083 PEDOT:PSS. Figure 3.10a shows the conductivity of these samples as a function of EG added and more data are provided in Table 5. For Al 4083 PEDOT:PSS, the conductivity was not increased until 5 vol% EG was added. For PEDOT-MEOH:PSS, however, even adding a small amount of EG resulted in a noticeable increase of the conductivity. The conductivity of PSS100-L increased dramatically from 0.034 to 0.057 S/m by adding 2 vol% of EG, and slightly increased to 0.061 and 0.063 S/m by adding 3 and 5 vol% of EG. The conductivity of PSS80-L and PSS60-L increased linearly with EG added, from 0.035 and 0.041 S/m of the pristine PSS80-L and PSS60-L, respectively, to 0.043 and 0.066 S/m of PSS80-L and PSS60-L treated with 5 vol% EG, respectively. Similar trend was observed for PSS100(80, 60)-H PEDOT-MeOH:PSS. A significant increase of conductivity from 0.041 to 0.063 S/m for PSS100-H by adding 3 vol% EG. The conductivity of PSS80-H and PSS60-H increased linearly with the adding of EG. Particularly, the conductivity of PSS80-H with 6 vol% EG reached 0.074 S/m.

We selected the PEDOT-MeOH:PSS synthesized with the high amount of ferric oxidizing agent (PSS100(80, 60)-H) as the model systems to investigate whether structural change and phase segregation play roles in the increase of conductivity of PEDOT-MeOH:PSS. We collected the Raman spectra and AFM images. Figure 3.10b shows the calculated ratios of quinoid to benzoid structure based on the peak area corresponding to the quinoid and benzoid C_α=C_β symmetric stretching (Fig. 3.11). The ratios of quinoid to benzoid structure increased with adding EG to PSS100(80, 60)-H PEDOT-MeOH:PSS, which even shows the same increasing trend as those in conductivity (Fig. 3.10a). For example, a big increase of the ratio of quinoid to benzoid structure exhibited when 3 vol% of EG was added to PSS100-H, corresponding to the big increase of the conductivity. Less increase of the ratio of quinoid to benzoid structure and conductivity by increasing EG from 3 to 5 vol% for PSS100-H and from 5 to 6 vol% for PSS80-H is probably because pristine PSS100-H and PSS80-H already have high contents of quinoid structure, therefore, a certain amount of EG may not induce further structural change. Nonetheless, we believed that the structural change of the PEDOT-MeOH:PSS backbone is one of the factors for the improvement of the conductivity of PEDOT-MeOH:PSS thin films.

We further studied the surface morphology of EG treated PEDOT-MeOH:PSS and selected PSS80-H as an example. Large area (10 × 10 μm^2) topographic AFM images (Fig. 3.12) show that large particles, presented on the pristine PSS80-H thin film surface, disappeared on the surfaces of PSS80-H treated with 2, 3, 5 and 6 vol% EG. The particles are most likely due to the clusters of short-chain PEDOT-MeOH polymers or coiled long-chain PEDOT-MeOH polymers that were not effectively doped by PSS. Adding EG and stirring the mixtures overnight made these PEDOT-MeOH having better interactions with PSS, and thereby dissolved in water. With more EG added, the surface morphology turned to nonuniform with more domain contrasts, especially, the surface of PSS80-H treated with 6 vol% EG (Fig. 3.12e), indicating phase segregations. Small area (1 × 1 μm^2) topographic AFM images of these films are shown in Fig. 3.10c. The pristine PSS80-H surface was smooth with more uniformly distributed fine PEDOT-MeOH and PSS domains. Adding 2, 3 and 5 vol% EG, the surfaces became rough with obvious brighter and darker domains. In addition, the brighter domains became larger with blurry domain boundaries. When 6 vol% of EG was added, it was difficult to acquire clear images and large bright domains were on the surface. These morphological changes are arbitrated to the segregation of PEDOT-MeOH and PSS phases caused by EG[43, 60, 62, 66, 67]. Because of the -MeOH group on PEDOT, EG can form hydrogen bonds with different PEDOT-MeOH chains, tightening them together, and thus segregating PEDOT-MeOH out from PSS. The tight packing of PEDOT-MeOH chains facilitate hole transport within

PEDOT-MeOH domains. In the meantime, segregated PEDOT-MeOH domains and PSS domains allow more efficient intra-domain hole transport. As a result, the conductivity was increased, which might be mainly due to the hole mobility increase.

Based on our Raman spectroscopic and AFM topographic image results, we believe that both the structural change from benzoid to quinoid and the phase segregation between PEDOT-MeOH and PSS domains caused the increase of the conductivity of PEDOT-MeOH:PSS with EG additive. The -MeOH group in PEDOT-MeOH, which can form hydrogen bonding with EG, makes the increase of the conductivity for PEDOT-MeOH:PSS more efficient than PEDOT:PSS. Additionally, because more uniform PEODT-MeOH and PSS domains are in pristine PEDOT-MeOH:PSS thin films, a small amount of EG can effectively promote phase segregation. Therefore, the electronic and morphological properties of PEDOT-MeOH:PSS can be more effectively tuned by EG additive.

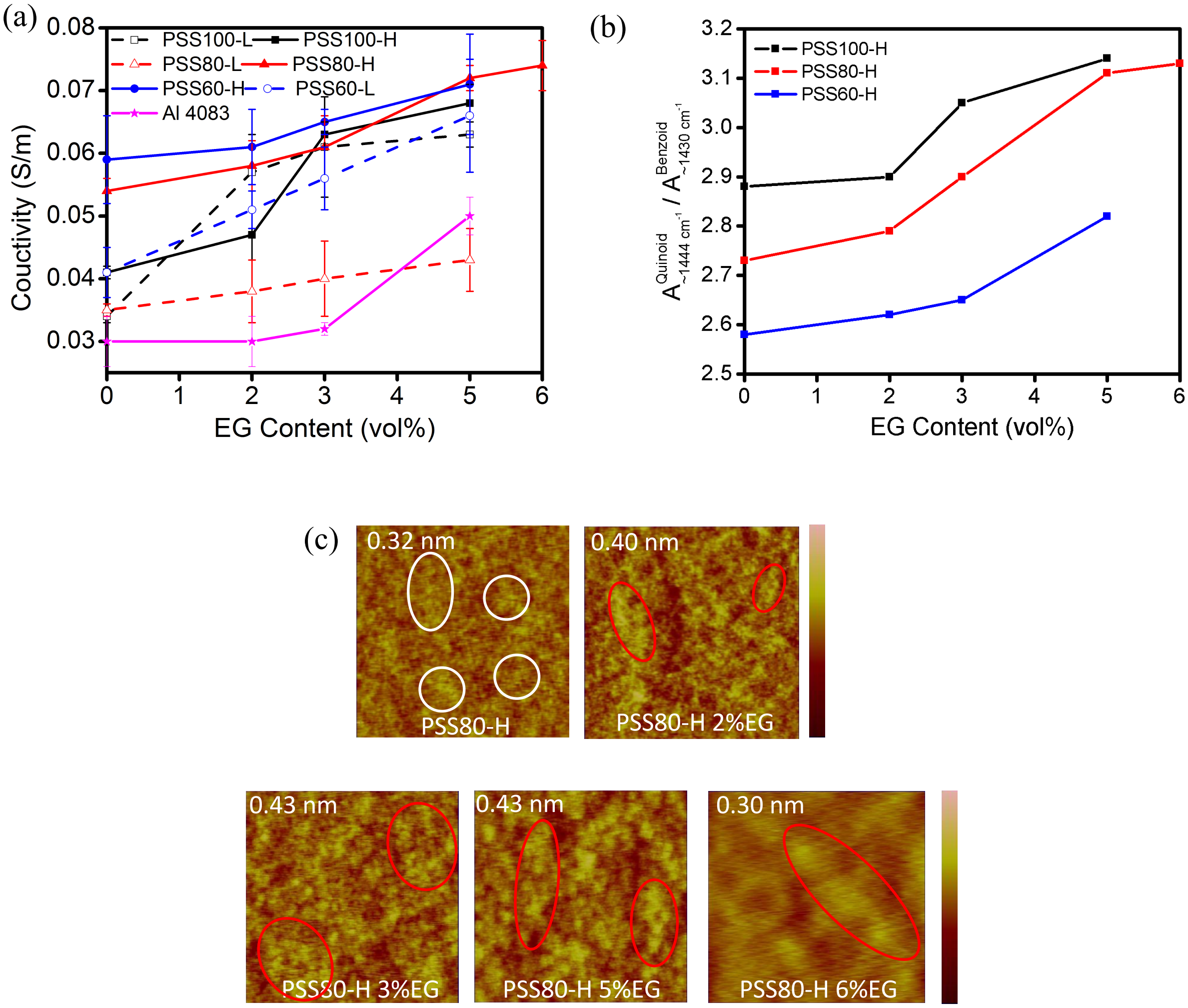

Figure 3.9 (a) Conductivity of PEDOT-MeOH:PSS and Al 4083 PEDOT:PSS as a function of EG added. (b) Quinoid to benzoid structural ratios of PSS100(80, 60)-H as a function of EG added. (c) Topographic AFM images (1 μm x 1 μm) of PSS80-H with different amount of EG added. The z-scale bar is 5 nm. The root mean square (RMS) roughness of the surface is shown on the top left corner of the corresponding image.

Table 5. Conductivity of Al 4083 PEDOT:PSS and PEDOT-MeOH:PSS thin films with different amount of ethylene glycol (EG) added.

Sample Code	Al4083			
EG (vol%)	0	2	3	5
Resistivity (Ω m)	38.16±6.35	32.82±6.35	31.70±0.43	20.17±1.21
Thickness (nm)	53.3±0.8	24.1±8.7	43.5±0.5	28.0±1.6
Conductivity (S/m)	0.030±0.004	0.030±0.004	0.032±0.001	0.050±0.003

Sample Code	PSS100-L			
EG (vol%)	0	2	3	5
Resistivity (Ω m)	29.80±0.26	17.53±2.23	16.43±2.91	15.94±0.31
Thickness (nm)	41.2±0.4	24.1±3.1	22.7±4.0	22.2±0.5
Conductivity (S/m)	0.034±0.001	0.057±0.006	0.061±0.008	0.063±0.002

Sample Code	PSS80-L			
EG (vol%)	0	2	3	5
Resistivity (Ω m)	28.77±0.94	26.62±4.56	24.72±4.78	23.07±2.73
Thickness (nm)	40.1±1.3	36.3±6.1	34.0±6.5	31.0±3.7
Conductivity (S/m)	0.035±0.001	0.038±0.005	0.040±0.006	0.043±0.005

Sample Code	PSS60-L			
EG (vol%)	0	2	3	5
Resistivity (Ω m)	24.45±3.32	19.72±1.38	18.01±1.89	15.10±2.69
Thickness (nm)	32.6±4.3	26.8±1.8	24.2±2.5	20.7±3.7
Conductivity (S/m)	0.041±0.004	0.051±0.003	0.056±0.005	0.066±0.009

Sample Code	PSS100-H			
EG (vol%)	0	2	3	5
Resistivity (Ω m)	24.23±0.25	21.46±1.68	15.78±0.51	14.77±0.68
Thickness (nm)	33.5±0.4	30.0±2.3	22.0±0.7	20.7±0.9
Conductivity (S/m)	0.041±0.001	0.047±0.004	0.063±0.002	0.068±0.003

Sample Code	PSS80-H				
EG (vol%)	0	2	3	5	6
Resistivity (Ω m)	18.49±0.39	17.34±1.16	16.31±1.41	13.84±0.32	13.46±0.41
Thickness (nm)	25.3±0.5	23.5±1.5	22.3±1.9	19.0±0.4	18.5±0.5
Conductivity (S/m)	0.054±0.002	0.058±0.004	0.061±0.005	0.072±0.002	0.074±0.004

Sample Code	PSS60-H			
EG (vol%)	0	2	3	5
Resistivity (Ω m)	16.87±2.31	16.39±2.07	15.49±0.37	14.11±1.82
Thickness (nm)	23.0±3.1	22.8±2.9	21.5±0.5	19.5±2.5
Conductivity (S/m)	0.059±0.007	0.061±0.006	0.065±0.002	0.071±0.008

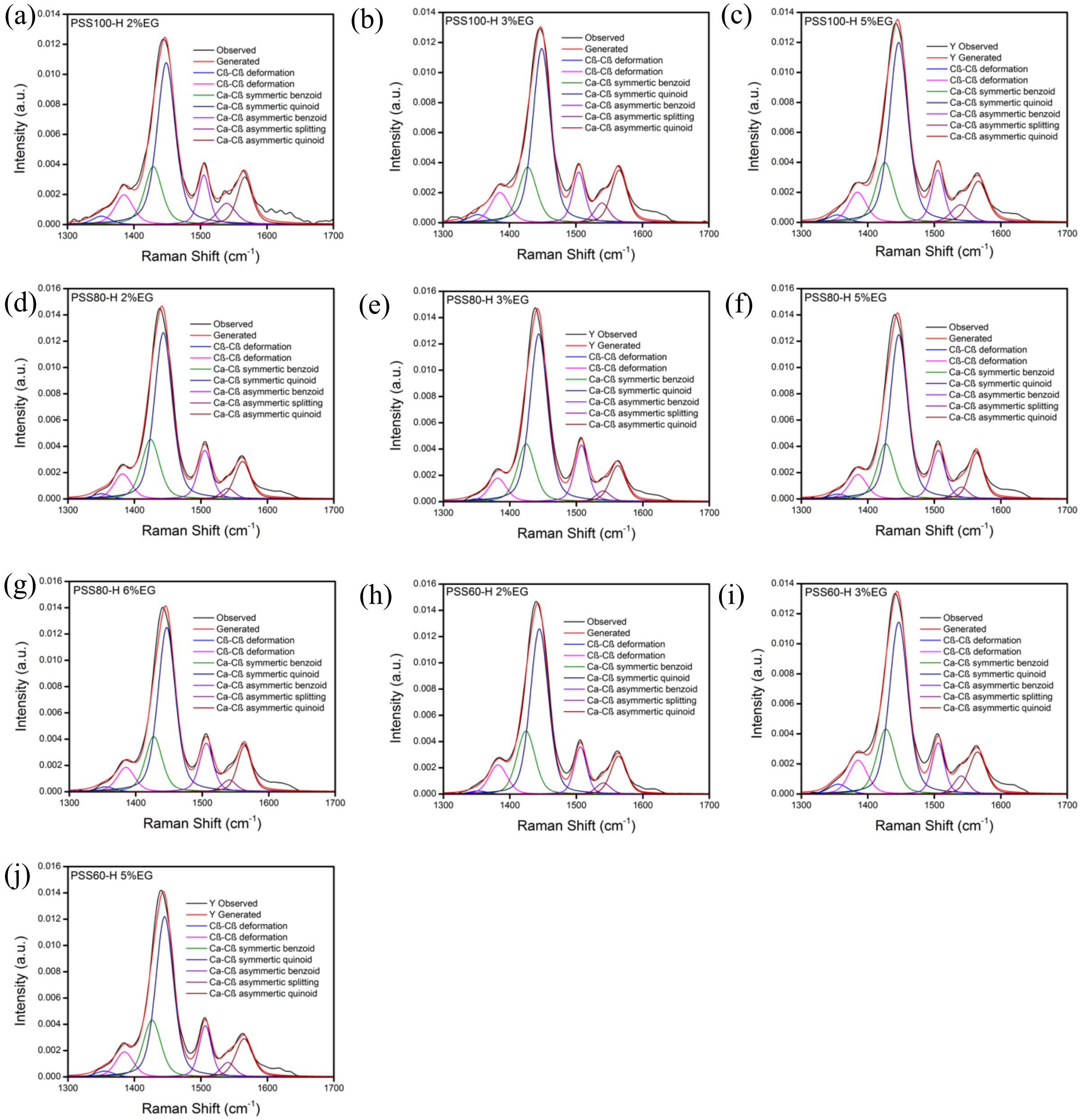

Figure 3.10 Deconvolution of Raman spectra of PSS100-H with (a) 2 vol% EG, (b) 3 vol% EG, (c) 5 vol% EG, PSS 80-H with (d) 2 vol% EG, (e) 3 vol% EG, (f) 5 vol% EG, (g) 6 vol% EG, and PSS60-H with (h) 2 vol% EG, (i) 3 vol% EG, (j) 5 vol% EG.

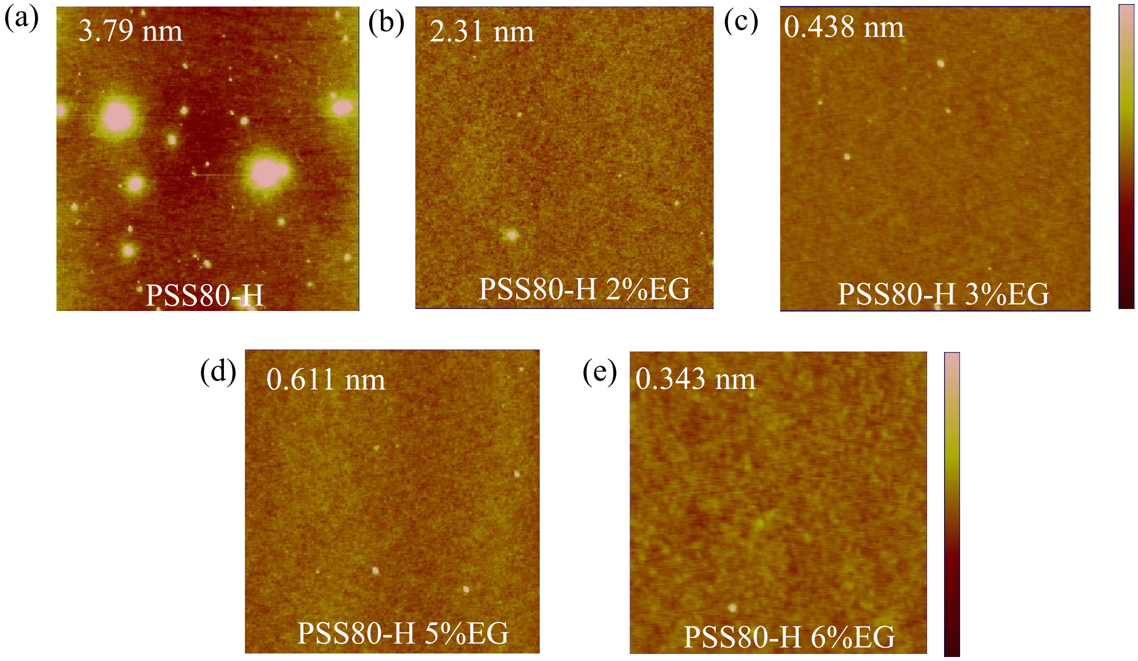

Figure 3.11 Large-scale ($10 \times 10\ \mu m^2$) topographic AFM images of PSS80-H, with (a) 0 vol% EG, (b) 2 vol% EG, (c) 3 vol% EG, (d) 5 vol% EG, (e) 6 vol% EG. The Z scale is 10 nm. The root mean square (RMS) roughness of the surface is shown on the top left corner of the corresponding image.

3.6. MAPbI3 PVSCs with HTLs Using EG Treated PEDOT-MEOH:PSS and PEDOT:PSS

We fabricated $MAPbI_3$ PVSCs using EG treated PEDOT-MeOH:PSS and PEDOT:PSS as HTLs. Figure 3.13 shows the average PCE, V_{oc}, J_{sc} and FF of all PVSCs. Figures 3.14-3.20 show the statistics of PCE, V_{oc}, J_{sc} and FF of PVSCs and the J-V curves of the best performance devices for using each PEDOT-MeOH:PSS and PEDOT:PSS treated with different amount of EG. The device characteristic parameters are summarized in Tables 6-12. The PVSCs with the EG treated Al 4083 PEDOT:PSS HTLs exhibited the decrease of average PCE's from 9.09% with the pristine PEDOT:PSS to 8.55, 8.87, and 7.93% with 2, 3 and 5 vol% EG treated PEDOT:PSS, respectively, which were mainly due to the reduced V_{oc}'s and J_{sc}'s even though slightly increased FF's (Fig. 3.13, Fig. 3.14 and Table 6). Despite that we did not measure the work function of EG treated PEDOT:PSS, previous work showed that PEDOT:PSS treated with sorbitol or glycerol exhibited the decrease of work function from ~5.2 eV of pristine PEDOT:PSS to ~5.05 eV with 5 wt% sorbitol or glycerol[68]. We speculated that the decreased V_{oc}'s and J_{sc}'s of PVSCs based on EG treated PEDOT:PSS are mainly due to the enlarged energy level mismatch of the work function of EG treated PEDOT:PSS and the valence band maximum of $MAPbI_3$.

The significantly increased PCEs were observed for some PVSCs based on EG treated PSS100(80,60)-H PEDOT-MeOH:PSS HTLs, which are mainly due to the increased J_{sc}'s. Several of them had better performance than the PVSCs based on PEDOT:PSS. The performance of PVSCs based on PSS60-H treated with 3 vol% EG overperformed those based on PEDOT:PSS, exhibiting the average PCE of 10.00% and the maximum PCE of 11.34%, due to the high average J_{sc} of 18.46 mA cm^{-2}, even though the average V_{oc} was 0.79 V and the average FF was 0.68 (Fig. 3.13, Fig. 3.15 and Table 7). The PVSCs based on PSS60-H treated with 2, 3 and 5 vol% EG generated the average J_{sc} of 17.38, 18.46, and 18.74 mA cm^{-2}, respectively, the highest J_{sc}'s among all the PVSCs, which could be attributed to the highest conductivities of these PEDOT-MeOH:PSS thin films (Fig. 3.13). PSS80-H treated with 3, 5, and 6 vol% EG as HTLs gave the PCE's of PVSCs to be 9.38, 11.08 and 10.81%, respectively, because of the average J_{sc} of 14.60, 15.10 and 14.64 mA cm^{-2}, respectively. The champion devices, exhibiting the maximum PCE's of 11.51 and 11.68%, contained the HTLs with PSS80-H treated with 5 and 6 vol% EG, respectively. Even though the thin films of PSS80-H treated with 5 and 6 vol% EG had the compatible conductivities as the thin film of PSS60-H treated with 5 vol% EG, the J_{sc}'s of PVSCs based on these EG treated PSS80-H HTLs were about 3 mA cm^{-2} lower than those based on EG treated PSS60-H, which indicating that other factors could play roles affecting the device performance. The ratio of quinoid to benzoid structure of the 5 and 6 vol% EG treated PSS80-H thin films were around 3.1 compared to 2.65 and 2.8 for 3 and 5 vol% EG treated PSS60-H, respectively (Fig. 3.10b). These structural differences may affect the charge extraction at the HTL/active layer interface, which could be the reason that the average V_{oc}'s of PVSCs based on 5 and 6 vol% EG treated PSS80-H around 1.01-1.02 V were much higher than the average V_{oc}'s of 0.79 and 0.67 V for 3 and 5 vol% EG treated PSS60-H, respectively. In addition, the higher V_{oc}'s might be due to the better energy alignment of the work function of PSS80-H treated with EG resulting from slightly lowered work function. It has been reported that the work function of PEDOT:PSS was lowered about 0.15 eV by treating with 5 wt% sorbitol or glycerol[68]. The dramatic impact of lowered work function on device performance due to EG treated PEDOT-MEOH:PSS was particularly demonstrated by the PVSCs based on EG treated PSS100-H HTLs. The work function of pristine PSS100-H is 5.5 eV, unfavorable alignment with $MAPbI_3$, and thus leading to the fluctuated V_{oc}'s and very low J_{sc}'s and FF's (Fig. 3.10). Treating with EG for PSS100-H offered greatly improved V_{oc}'s, J_{sc}'s, and

FF's of PVSCs (Fig. 3.17 and Table 9). The PVSCs based on PSS100-H treated with 3 vol% EG exhibited an average PCE of 9.56% because of the greatly increased average V_{oc} of 1.01 V, FF of 0.60 and J_{sc} of 15.83 mA cm^{-2}.

All PVSCs based on EG treated PSS60-L and PSS80-L PEDOT-MeOH:PSS HTLs exhibited better performance than those based on the pristine PSS60-L and PSS80-L HTLs, mainly due to the increased J_{sc}'s (Fig. 3.13, Fig 3.18-3.19 and Table 10-11). The device performance was only shown a slightly improved for those based on 2 vol% EG treated PSS100-L, but lowered performance for those PVSCs based on 5 and 6 vol% EG treated PSS100-L (Fig. 3.13, Fig 3.20 and Table 13). Relatively stable V_{oc}'s and FF's might be due to the short-chain PEDOT-MeOH polymers in these samples. Adding EG may easily cause the structural change because of the higher mobility of short-chain PEDOT-MeOH, which increased conductivity (Fig. 3.10a), but may not cause a significant PEOT-MeOH and PSS phase segregation because the short-chain PEDOT-MeOH may still stay within PSS shells, which had no obvious influence to V_{oc}'s and FF's.

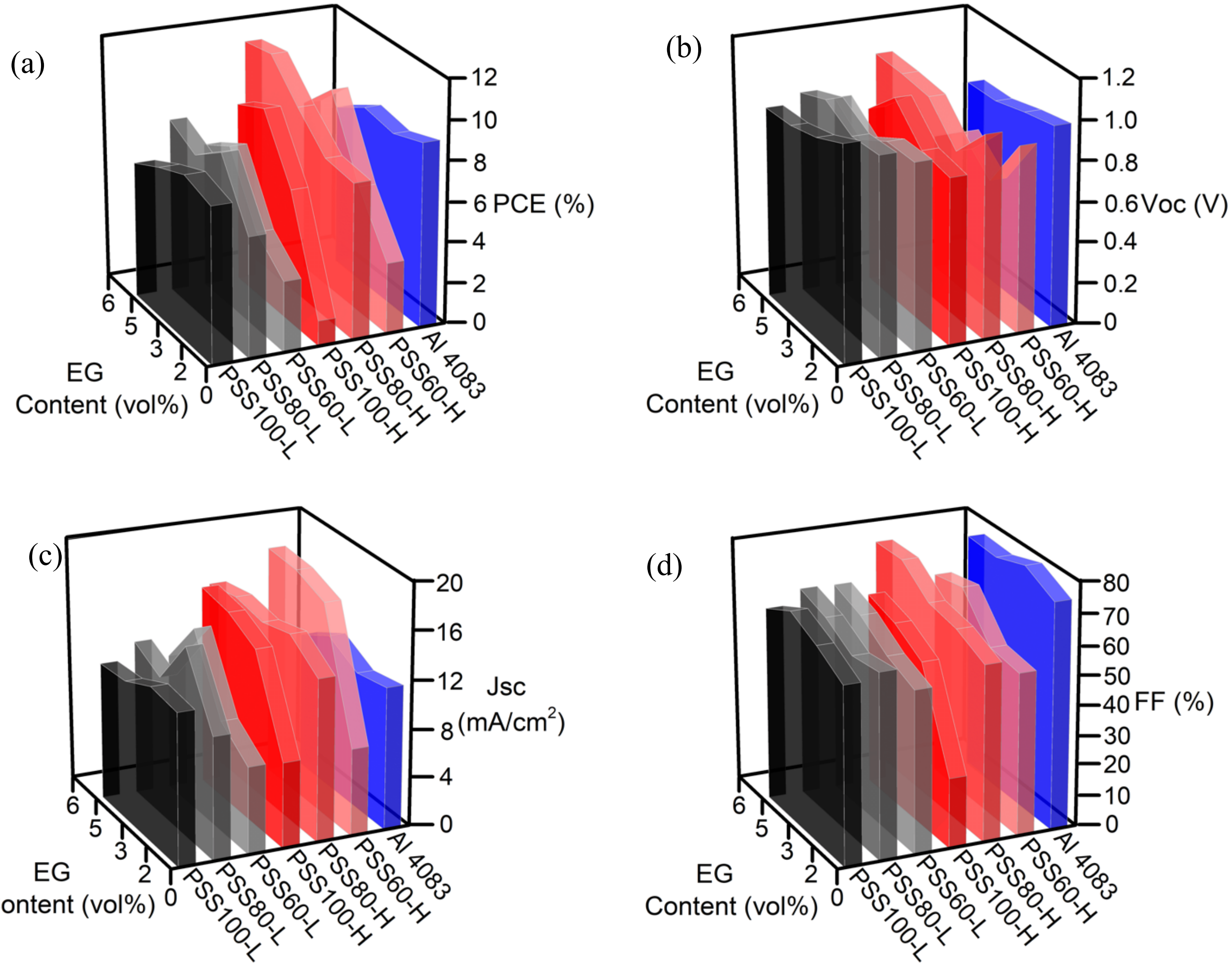

Figure 3.12 Statistics of (a) PCE, (b) Voc, (c) Jsc, and (d) FF of the devices based on PEDOT:PSS or PEDOT-MeOH:PSS with or without EG.

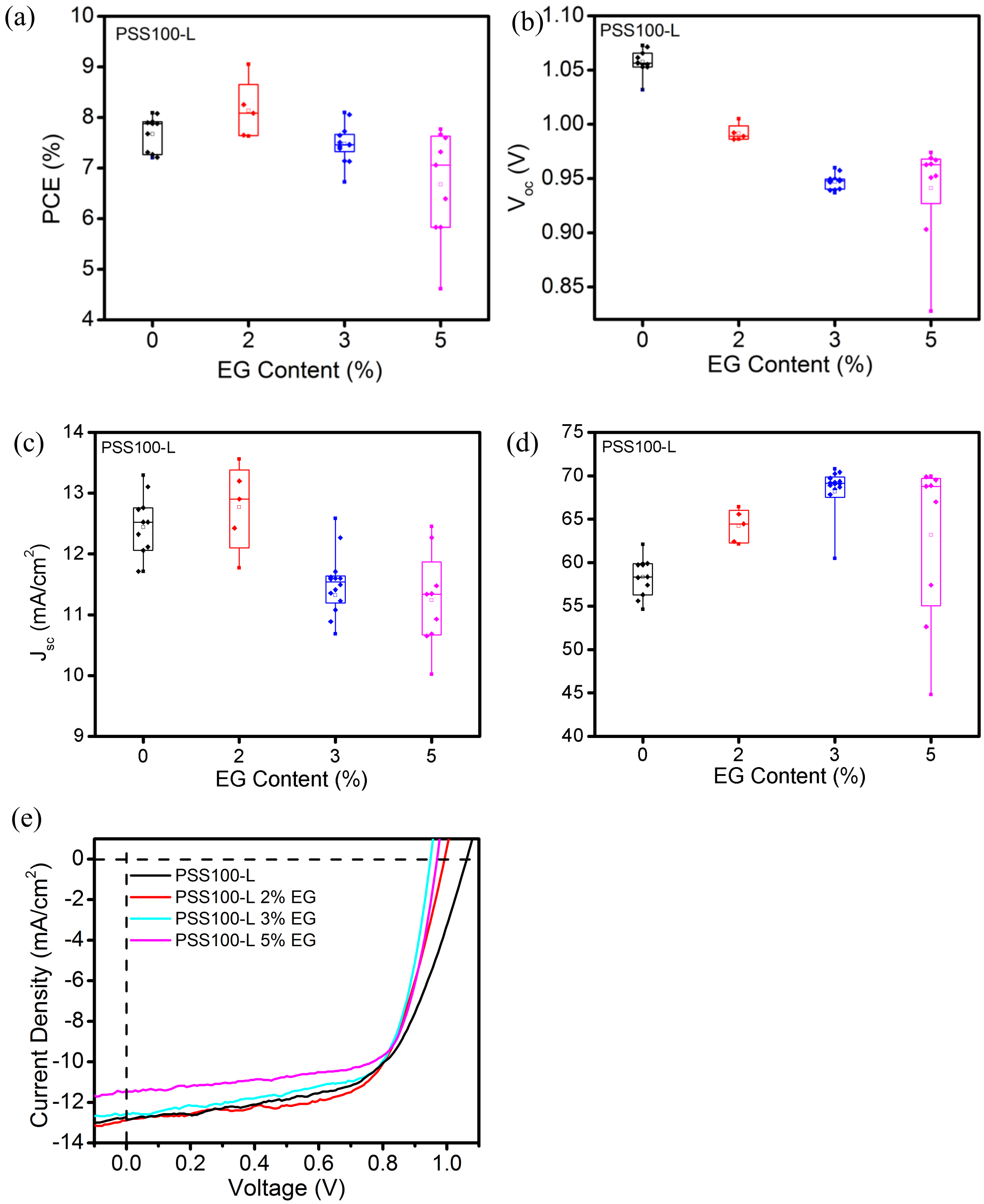

Figure 3.13 Statistics of (a) PCE, (b) Voc, (c) Jsc, and (d) FF of the devices based on PSS100-L with or without EG. (e) J-V curve of the device with the best performance based on pristine PSS100-L with 2 vol%, 3 vol% and 5 vol% EG.

Table 6. Device performance summary of the devices based on Al 4083 PEDOT:PSS with and without EG.

HTL	Voc (V)	Jsc (mA/cm^2)	FF (%)	PCE (%)	PCE$_{Max}$ (%)
Al 4083	0.99±0.01	11.69±0.75	74.3±1.7	9.09±0.46	9.53
Al 4083 w/ 2 vol% EG	0.96±0.01	11.20±0.23	79.8±0.2	8.55±0.14	8.65
Al 4083 w/ 3 vol% EG	0.92±0.01	12.62±0.71	76.4±3.9	8.87±0.41	9.42
Al 4083 w/ 5 vol% EG	0.92±0.01	11.09±0.43	77.4±1.2	7.93±0.25	8.16

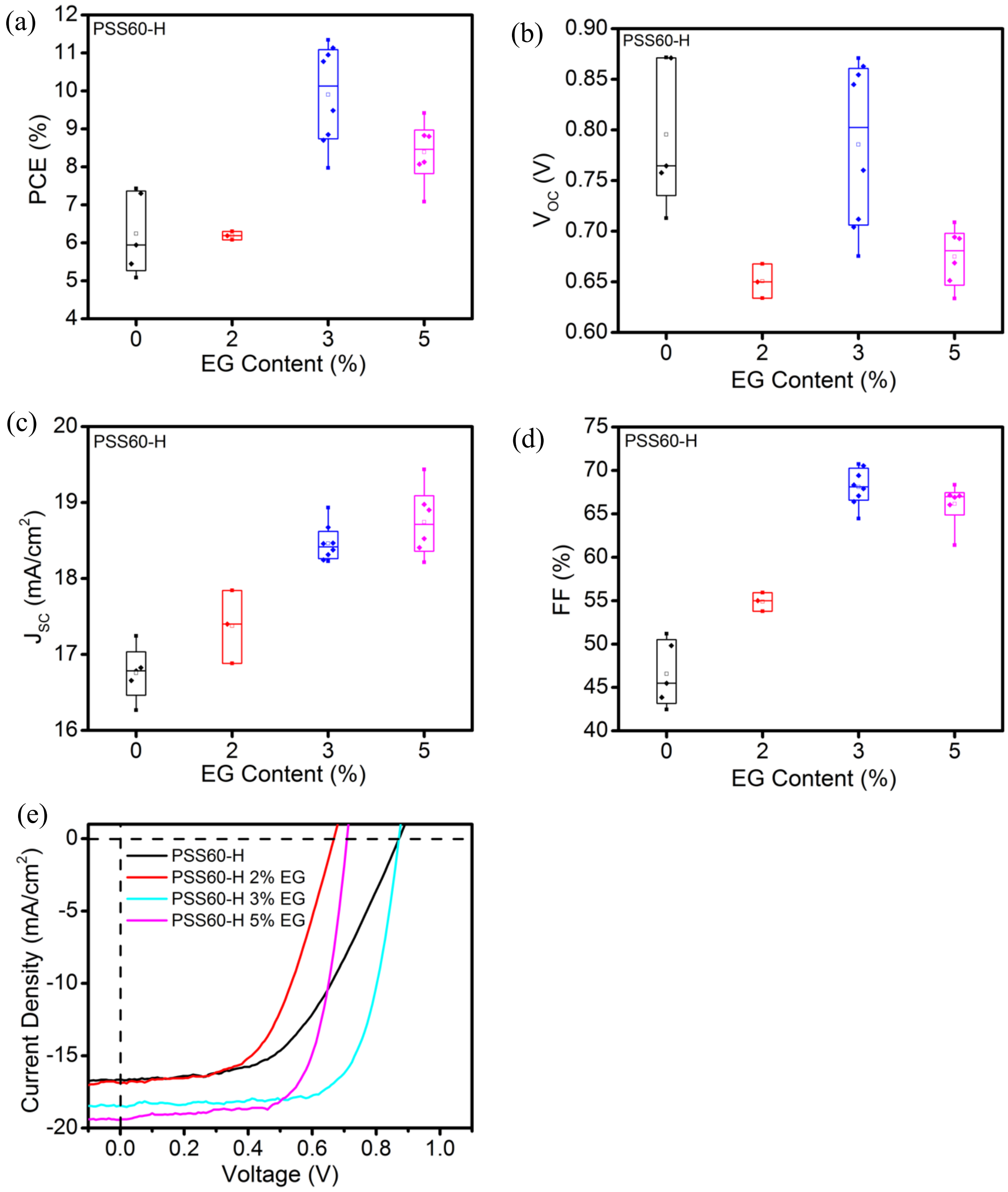

Figure 3.14 Statistics of (a) PCE, (b) V_{oc}, (c) J_{sc}, and (d) FF of the devices based on PSS60-H with and without EG. (e) J-V curves of the devices with the best performance based on pristine PSS60-H and PSS60-H with 2 vol%, 3 vol% and 5 vol% EG.

Table 7. Device performance summary of the devices based on PSS60-H with or without EG.

HTL	Voc (V)	Jsc (mA/cm^2)	FF (%)	PCE (%)	PCE$_{Max}$ (%)
PSS60-H	0.92±0.01	7.13±0.58	53.2±1.6	3.47±0.24	3.90
PSS60-H w/ 2 vol% EG	0.65±0.02	17.38±0.48	54.9±1.1	6.19±0.11	6.30
PSS60-H w/ 3 vol% EG	0.79±0.08	18.46±0.22	68.2±2.0	10.00±1.25	11.34
PSS60-H w/ 5 vol% EG	0.67±0.03	18.74±0.45	66.2±2.5	8.39±0.81	9.42

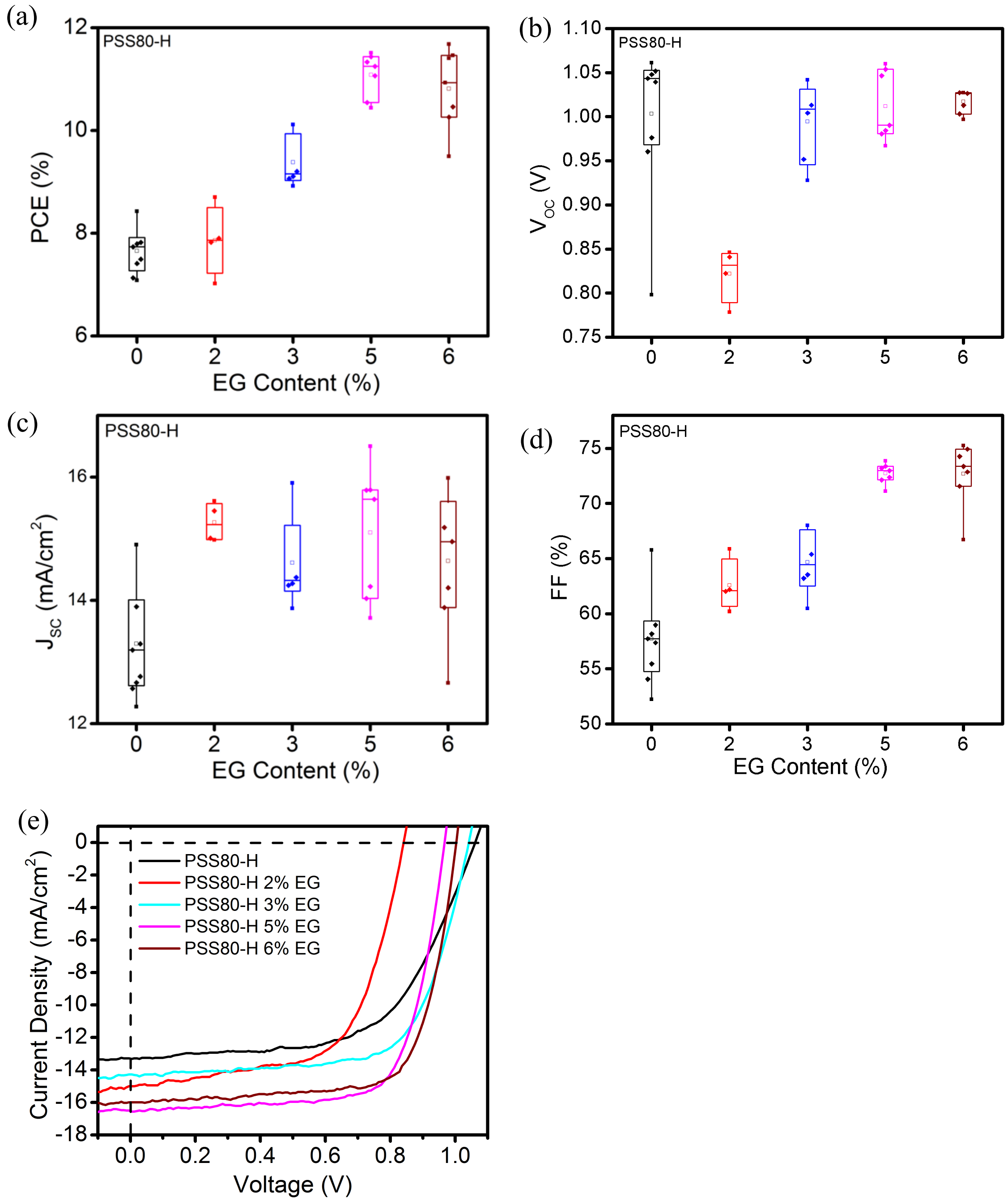

Figure 3.15 Statistics of (a) PCE, (b) V_{oc}, (c) J_{sc}, and (d) FF of the devices based on PSS80-H with and without EG. (e) *J-V* curves of the devices with the best performance based on pristine PSS80-H and PSS80-H with 2 vol%, 3 vol%, 5 vol% and 6 vol% EG.

Table 8. Device performance summary of the devices based on PSS80-H with and without EG.

HTL	Voc (V)	Jsc (mA/cm^2)	FF (%)	PCE (%)	PCE$_{Max}$ (%)
PSS80-H	1.00±0.08	13.30±1.44	57.7±3.6	7.66±0.40	8.43
PSS80-H w/ 2 vol% EG	0.82±0.03	15.26±0.31	62.6±2.4	7.86±0.69	8.70
PSS80-H w/ 3 vol% EG	0.99±0.04	14.60±0.73	64.7±2.9	9.38±0.49	10.11
PSS80-H w/ 5 vol% EG	1.01±0.04	15.10±1.08	72.7±0.9	11.08±0.43	11.51
PSS80-H w/ 6 vol% EG	1.02±0.02	14.64±1.14	72.7±2.9	10.81±0.79	11.68

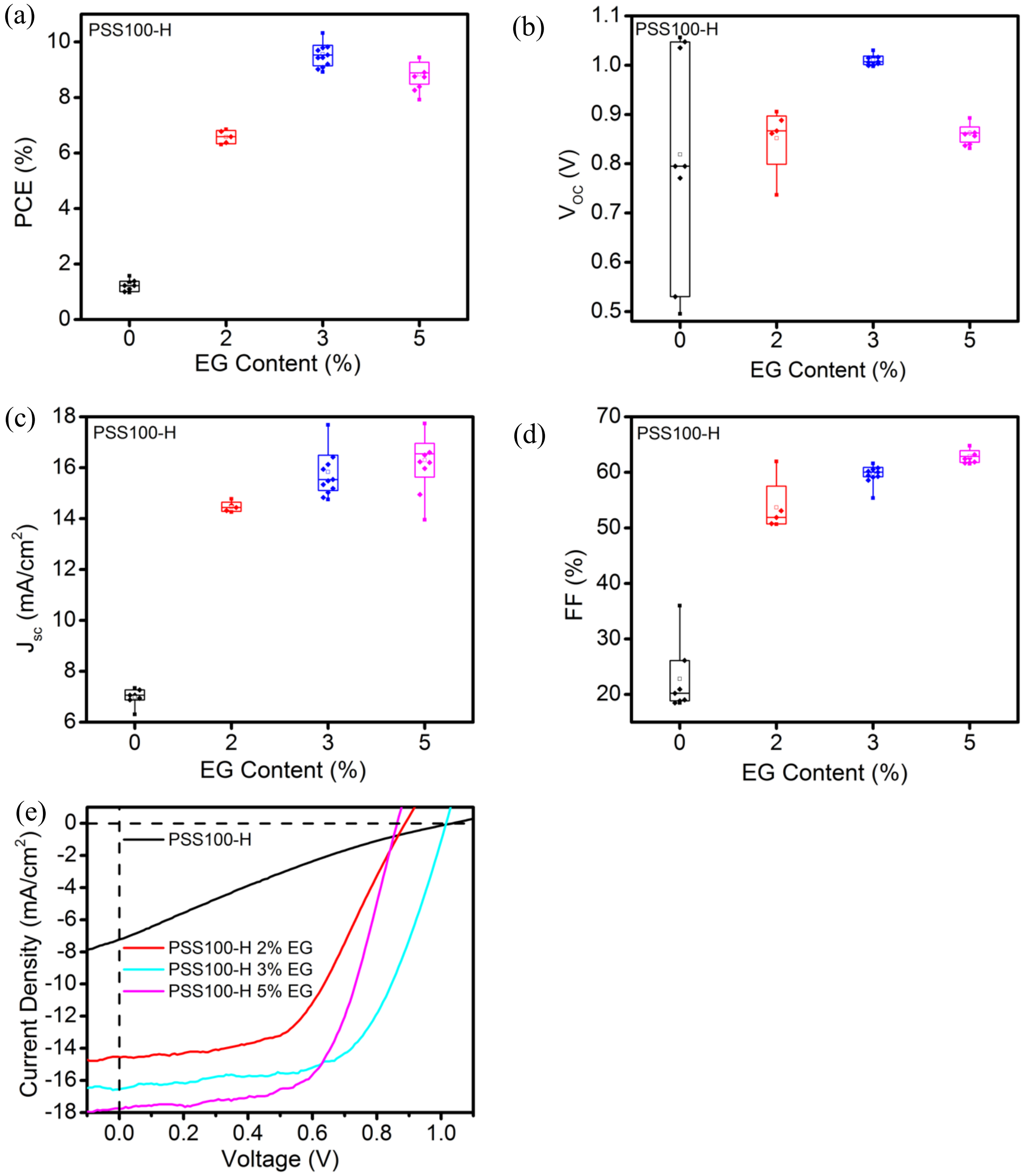

Figure 3.16 Statistics of (a) PCE, (b) Voc, (c) Jsc, and (d) FF of the devices based on PSS100-H with and without EG. (e) J-V curves of the devices with the best performance based on pristine PSS100-H and PSS100-H with 2 vol%, 3 vol% and 5 vol% EG.

Table 9. Device performance summary of the devices based on PSS100-H with and without EG.

HTL	Voc (V)	Jsc (mA/cm^2)	FF (%)	PCE (%)	PCE$_{Max}$ (%)
PSS100-H	0.82±0.24	6.98±0.34	22.8±6.3	1.23±0.22	1.35
PSS100-H w/ 2 vol% EG	0.85±0.07	14.46±0.20	53.7±4.7	6.58±0.24	6.77
PSS100-H w/ 3 vol% EG	1.01±0.01	15.83±0.88	59.8±1.6	9.56±0.43	10.32
PSS100-H w/ 5 vol% EG	0.86±0.02	16.30±1.00	62.9±1.1	8.83±0.46	9.44

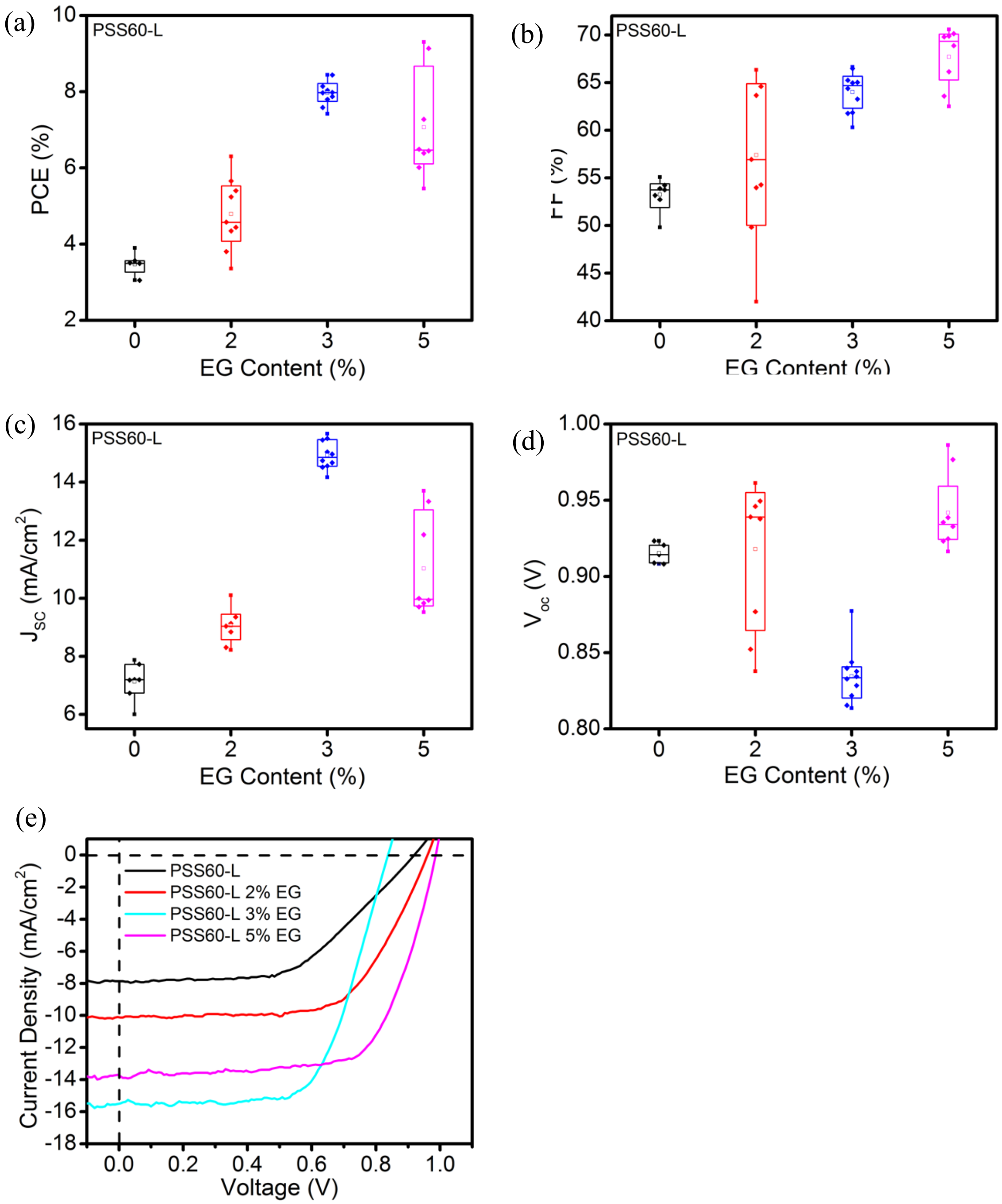

Figure 3.17 Statistics of (a) PCE, (b) V_{oc}, (c) J_{sc}, and (d) FF of the devices based on PSS60-L with and without EG. (e) *J-V* curves of the devices with the best performance based on pristine PSS60-L and PSS60-L with 2 vol%, 3 vol% and 5 vol% EG.

Table 10. Device performance summary of the devices based on PSS60-L with and without EG.

HTL	Voc (V)	Jsc (mA/cm^2)	FF (%)	PCE (%)	PCE$_{Max}$ (%)
PSS60-L	0.92±0.01	7.13±0.58	53.2±1.6	3.47±0.24	3.90
PSS60-L w/ 2 vol% EG	0.92±0.05	9.06±0.59	57.4±8.3	4.79±0.94	6.30
PSS60-L w/ 3 vol% EG	0.83±0.02	14.93±0.49	64.0±2.1	7.97±0.33	8.44
PSS60-L w/ 5 vol% EG	0.94±0.03	11.03±1.75	67.7±3.2	7.06±1.42	9.30

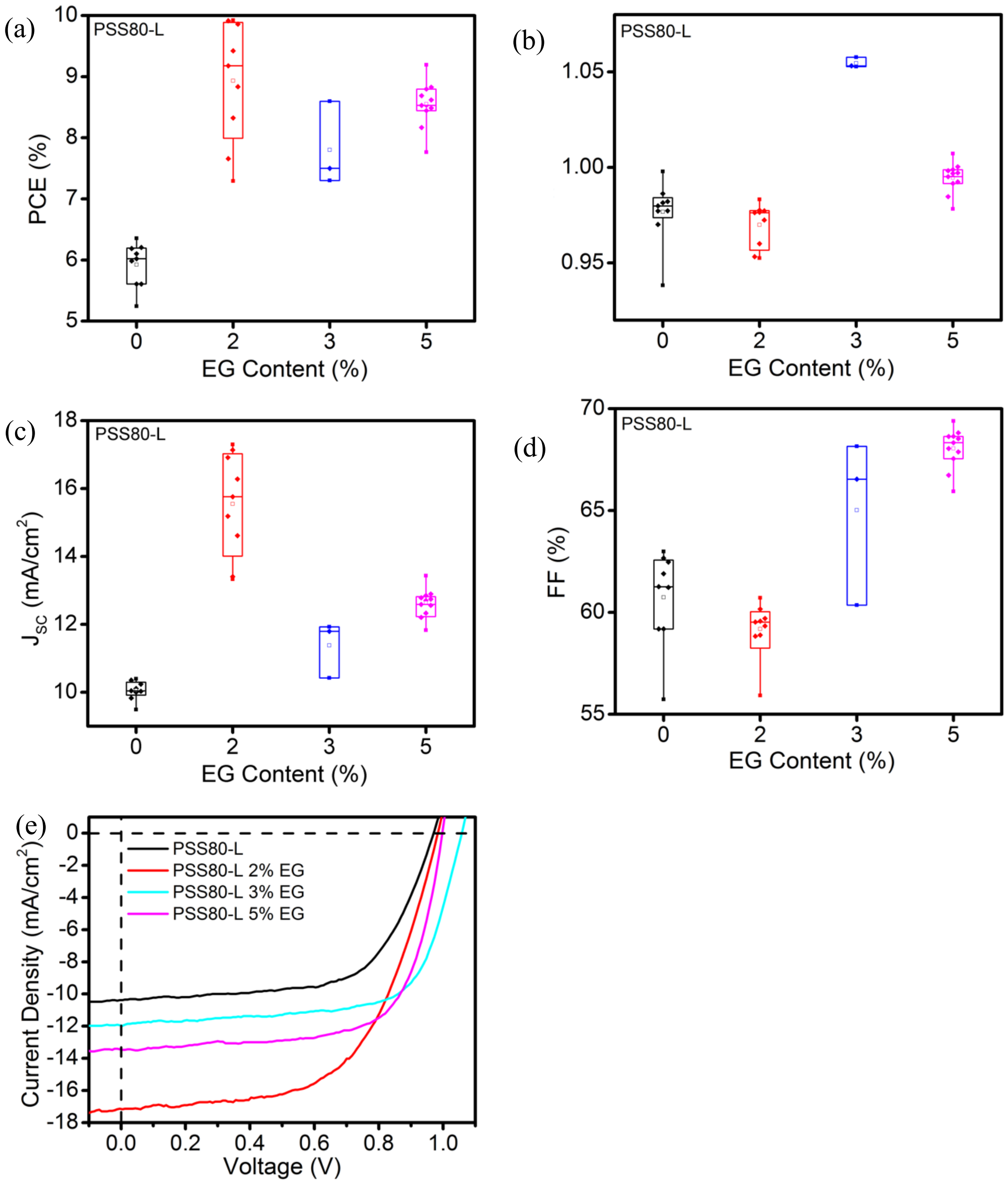

Figure 3.18 Statistics of (a) PCE, (b) V_{oc}, (c) J_{sc}, and (d) FF of the devices based on PSS80-L with and without EG. (e) *J*-*V* curves of the devices with the best performance based on pristine PSS80-L and PSS80-L with 2 vol%, 3 vol% and 5 vol% EG.

Table 11. Device performance summary of the devices based on PSS80-L with and without EG.

HTL	Voc (V)	Jsc (mA/cm^2)	FF (%)	PCE (%)	PCE$_{Max}$ (%)
PSS80-L	0.98±0.02	10.06±0.26	60.7±2.2	5.92±0.34	6.35
PSS80-L w/ 2 vol% EG	0.97±0.01	15.55±1.52	59.2±1.4	8.93±0.99	9.92
PSS80-L w/ 3 vol% EG	1.05±0.01	11.38±0.68	65.0±4.3	7.80±0.57	8.60
PSS80-L w/ 5 vol% EG	0.99±0.01	12.63±0.40	68.0±0.9	8.55±0.35	9.19

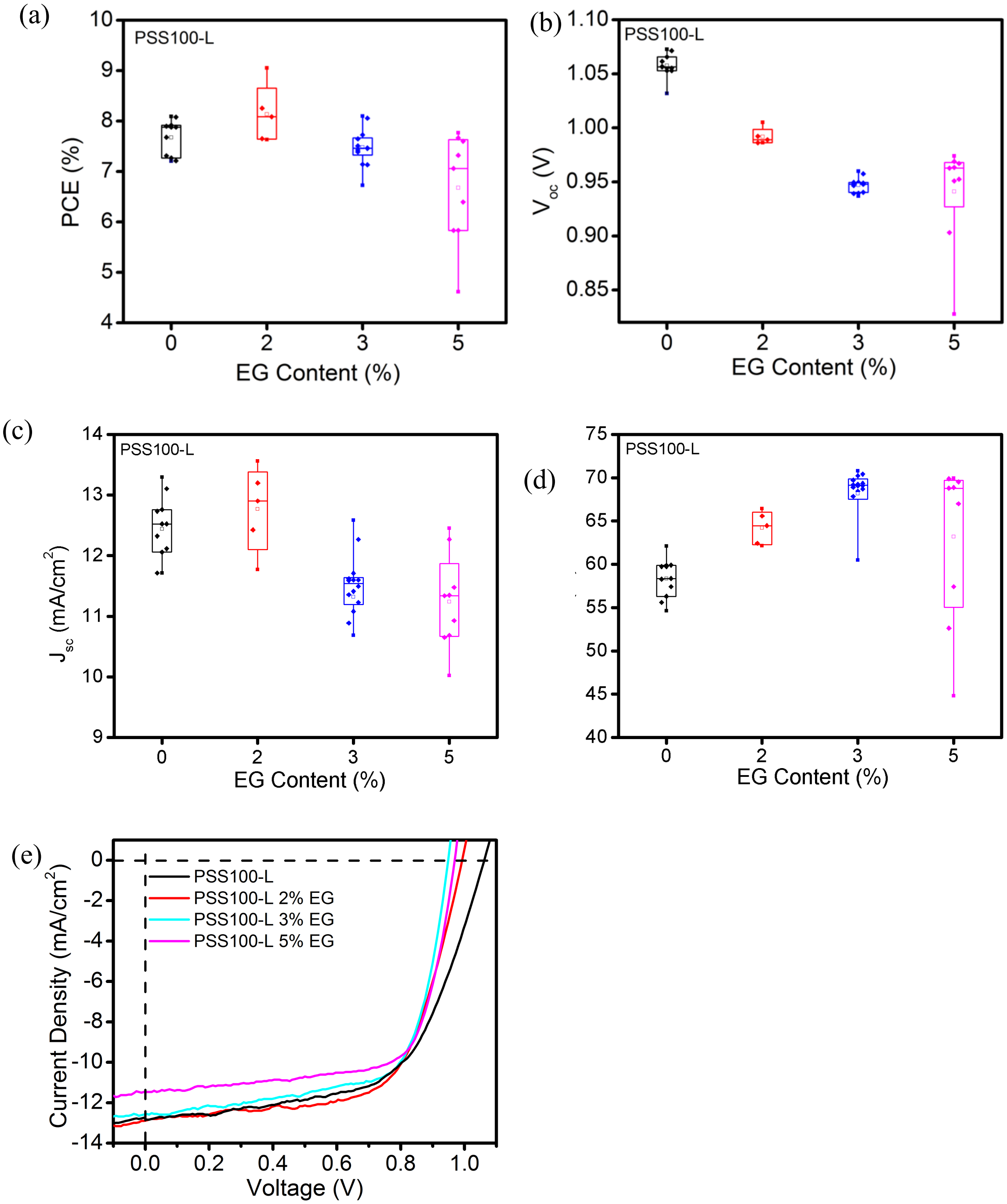

Figure 3.19 Statistics of (a) PCE, (b) V_{oc}, (c) J_{sc}, and (d) FF of the devices based on PSS100-L with and without EG. (e) J-V curves of the devices with the best performance based on pristine PSS100-L and PSS100-L with 2 vol%, 3 vol% and 5 vol% EG.

Table 12. Device performance summary of the devices based on PSS100-L with and without EG.

HTL	Voc (V)	Jsc (mA/cm^2)	FF (%)	PCE (%)	PCE$_{Max}$ (%)
PSS100-L	1.06±0.01	12.44±0.49	58.4±2.1	7.68±0.34	8.09
PSS100-L w/ 2 vol% EG	0.99±0.01	12.77±0.62	64.2±1.7	8.14±0.52	9.05
PSS100-L w/ 3 vol% EG	0.95±0.01	11.51±0.48	68.7±2.4	7.48±0.34	8.10
PSS100-L w/ 5 vol% EG	0.94±0.04	11.24±0.73	63.2±8.8	6.68±1.02	7.77

Chapter 4. Conclusions

In summary, we synthesized a hole transport material based on PEDOT-MeOH:PSS for PVSCs and tuned its conductivity and WF by changing the amount of PSS and ferric catalyst used in the polymerization reaction. It was found that increasing amount of PSS and ferric catalyst can enhance the conductivity and enlarge the WF of the PEDOT-MeOH:PSS thin film. EG was used as the additive to further improve the conductivity of PEDOT-MeOH:PSS. The effects of EG on the PEDOT-MeOH:PSS HTL were to change the structure of PEDOT-MeOH backbone from benzoid to quinoid and to promote the phase segregation between PEDOT-MeOH and PSS domains. By fabricating and characterizing the perovskite solar cell devices, we demonstrated that more matched energy level between the WF of PEDOT-MeOH:PSS based HTL and VBM of $MAPbI_3$ perovskite can enhance the V_{oc} of the PVSCs, while the J_{sc} of the PVSCs can be modulated by the conductivity and WF of the PEDOT-MeOH:PSS based HTL. EG can enhance the conductivity but decrease the WF of the HTL, and using the appropriate amount of EG to modify the PEDOT-MeOH:PSS based HTL can significantly enhance the device performance of PVSCs.

References

1. Y. Li, L. Ji, R. G. Liu, C. X. Zhang, C. H. Mak, X. L. Zou, H. H. Shen, S. Y. Leu and H. Y. Hsu, *J Mater Chem A*, 2018, **6**, 12842-12875.
2. N.-G. J. M. t. Park, 2015, **18**, 65-72.
3. Q. Jiang, Y. Zhao, X. Zhang, X. Yang, Y. Chen, Z. Chu, Q. Ye, X. Li, Z. Yin and J. J. N. P. You, 2019, 1.
4. O. PV, https://www.oxfordpv.com/news/oxford-pv-perovskite-solar-cell-achieves-28-efficiency.
5. S. De Wolf, J. Holovsky, S. J. Moon, P. Loper, B. Niesen, M. Ledinsky, F. J. Haug, J. H. Yum and C. Ballif, *J Phys Chem Lett*, 2014, **5**, 1035-1039.
6. S. D. Stranks, G. E. Eperon, G. Grancini, C. Menelaou, M. J. P. Alcocer, T. Leijtens, L. M. Herz, A. Petrozza and H. J. Snaith, *Science*, 2013, **342**, 341-344.
7. C. Wehrenfennig, G. E. Eperon, M. B. Johnston, H. J. Snaith and L. M. J. A. m. Herz, 2014, **26**, 1584-1589.
8. M. I. H. Ansari, A. Qurashi, M. K. J. J. o. P. Nazeeruddin and P. C. P. Reviews, 2018, **35**, 1-24.
9. L. Meng, J. B. You, T. F. Guo and Y. Yang, *Accounts Chem Res*, 2016, **49**, 155-165.
10. W. S. Yang, B. W. Park, E. H. Jung, N. J. Jeon, Y. C. Kim, D. U. Lee, S. S. Shin, J. Seo, E. K. Kim, J. H. Noh and S. I. Seok, *Science*, 2017, **356**, 1376-+.
11. J. Y. Seo, R. Uchida, H. S. Kim, Y. Saygili, J. S. Luo, C. Moore, J. Kerrod, A. Wagstaff, M. Eklund, R. McIntyre, N. Pellet, S. M. Zakeeruddin, A. Hagfeldt and M. Gratzel, *Adv Funct Mater*, 2018, **28**.
12. W. S. Yang, J. H. Noh, N. J. Jeon, Y. C. Kim, S. Ryu, J. Seo and S. I. Seok, *Science*, 2015, **348**, 1234-1237.
13. H. Shi, C. C. Liu, Q. L. Jiang and J. K. Xu, *Adv Electron Mater*, 2015, **1**.
14. K.-G. Lim, S. Ahn, Y.-H. Kim, Y. Qi, T.-W. J. E. Lee and E. Science, 2016, **9**, 932-939.
15. N. J. Jeon, H. Na, E. H. Jung, T. Y. Yang, Y. G. Lee, G. Kim, H. W. Shin, S. I. Seok, J. Lee and J. Seo, *Nat Energy*, 2018, **3**, 682-+.
16. H. R. Tan, A. Jain, O. Voznyy, X. Z. Lan, F. P. G. de Arquer, J. Z. Fan, R. Quintero-Bermudez, M. J. Yuan, B. Zhang, Y. C. Zhao, F. J. Fan, P. C. Li, L. N. Quan, Y. B. Zhao, Z. H. Lu, Z. Y. Yang, S. Hoogland and E. H. Sargent, *Science*, 2017, **355**, 722-726.
17. H. L. Yip and A. K. Y. Jen, *Energ Environ Sci*, 2012, **5**, 5994-6011.
18. Q. S. Wei, M. Mukaida, Y. Naitoh and T. Ishida, *Adv Mater*, 2013, **25**, 2831-2836.
19. C. Bi, Q. Wang, Y. C. Shao, Y. B. Yuan, Z. G. Xiao and J. S. Huang, *Nat Commun*, 2015, **6**.
20. W. Shockley and H. J. Queisser, *J Appl Phys*, 1961, **32**, 510-&.
21. J. P. Correa-Baena, W. Tress, K. Domanski, E. H. Anaraki, S. H. Turren-Cruz, B. Roose, P. P. Boix, M. Gratzel, M. Saliba, A. Abate and A. Hagfeldt, *Energ Environ Sci*, 2017, **10**, 1207-1212.
22. C. C. Chueh, C. Z. Li and A. K. Y. Jen, *Energ Environ Sci*, 2015, **8**, 1160-1189.
23. T. Leijtens, G. E. Eperon, A. J. Barker, G. Grancini, W. Zhang, J. M. Ball, A. R. S. Kandada, H. J. Snaith and A. Petrozza, *Energ Environ Sci*, 2016, **9**, 3472-3481.
24. A. Elschner, S. Kirchmeyer, W. Lovenich, U. Merker and K. Reuter, *PEDOT: principles and applications of an intrinsically conductive polymer*, CRC Press, 2010.

25. J. H. Noh, S. H. Im, J. H. Heo, T. N. Mandal and S. I. Seok, *Nano Lett*, 2013, **13**, 1764-1769.
26. M. Wolf and H. J. A. e. c. Rauschenbach, 1963, **3**, 455-479.
27. K. J. Hong, S. T. Tan, K. K. Chong, C. C. Yap, M. H. H. Jumali and Y. L. Loo, *Renew Energ*, 2019, **135**, 589-596.
28. X. Huang, K. Wang, C. Yi, T. Y. Meng and X. Gong, *Adv Energy Mater*, 2016, **6**.
29. U. Wurfel, D. Neher, A. Spies and S. Albrecht, *Nat Commun*, 2015, **6**.
30. T. W. Lee and Y. S. Chung, *Adv Funct Mater*, 2008, **18**, 2246-2252.
31. J. Kim, C. Park, S. Im, H. Lee and J. H. Kim, *Rsc Adv*, 2019, **9**, 4028-4034.
32. T. Horii, H. Hikawa, M. Katsunuma and H. Okuzaki, *Polymer*, 2018, **140**, 33-38.
33. Q. Wang, C. C. Chueh, M. Eslamian and A. K. Y. Jen, *Acs Appl Mater Inter*, 2016, **8**, 32068-32076.
34. D. Huang, T. Goh, L. McMillon-Brown, J. Kong, Y. F. Zheng, J. Zhao, Y. Li, S. L. Zhao, Z. Xu and A. D. Taylor, *Acs Appl Mater Inter*, 2018, **10**, 25329-25336.
35. D. Huang, T. Goh, J. Kong, Y. F. Zheng, S. L. Zhao, Z. Xu and A. D. Taylor, *Nanoscale*, 2017, **9**, 4236-4243.
36. J. Huang, K. X. Wang, J. J. Chang, Y. Y. Jiang, Q. S. Xiao and Y. Li, *J Mater Chem A*, 2017, **5**, 13817-13822.
37. Q. F. Xue, M. Y. Liu, Z. C. Li, L. Yan, Z. C. Hu, J. W. Zhou, W. Q. Li, X. F. Jiang, B. M. Xu, F. Huang, Y. Li, H. L. Yip and Y. Cao, *Adv Funct Mater*, 2018, **28**.
38. J. Huang, C. H. Wang, Z. Y. Liu, X. Q. Qiu, J. L. Yang and J. J. Chang, *J Mater Chem C*, 2018, **6**, 2311-2318.
39. B. J. Richardson, L. Zhu, Q. J. S. E. M. Yu and S. Cells, 2013, **116**, 252-261.
40. N. Ahn, S. M. Kang, J. W. Lee, M. Choi and N. G. Park, *J Mater Chem A*, 2015, **3**, 19901-19906.
41. *United States Pat.,* 9892859, 2018.
42. Y. H. Ha, N. Nikolov, S. K. Pollack, J. Mastrangelo, B. D. Martin and R. Shashidhar, *Adv Funct Mater*, 2004, **14**, 615-622.
43. J. Ouyang, Q. F. Xu, C. W. Chu, Y. Yang, G. Li and J. Shinar, *Polymer*, 2004, **45**, 8443-8450.
44. N. Massonnet, A. Carella, O. Jaudouin, P. Rannou, G. Laval, C. Celle and J. P. Simonato, *J Mater Chem C*, 2014, **2**, 1278-1283.
45. R. Chen, K. Sun, Q. Zhang, Y. L. Zhou, M. Li, Y. Y. Sun, Z. Wu, Y. Y. Wu, X. L. Li, J. L. Xi, C. Ma, Y. Y. Zhang and J. Y. Ouyang, *Iscience*, 2019, **12**, 66-+.
46. L. Q. Ouyang, M. J. Jafari, W. Z. Cai, L. E. Aguirre, C. F. Wang, T. Ederth and O. Inganas, *J Mater Chem C*, 2018, **6**, 654-660.
47. H. Park, S. H. Lee, F. S. Kim, H. H. Choi, I. W. Cheong and J. H. Kim, *J Mater Chem A*, 2014, **2**, 6532-6539.
48. J. M. G. Cowie and V. Arrighi, *Polymers: chemistry and physics of modern materials*, CRC press, 2007.
49. R. Gangopadhyay, B. Das and M. R. J. R. A. Molla, 2014, **4**, 43912-43920.
50. L. Y. Park, D. Ofer, T. J. Gardner, R. R. Schrock and M. S. Wrighton, *Chem Mater*, 1992, **4**, 1388-1395.
51. K. Sun, S. P. Zhang, P. C. Li, Y. J. Xia, X. Zhang, D. H. Du, F. H. Isikgor and J. Y. Ouyang, *J Mater Sci-Mater El*, 2015, **26**, 4438-4462.
52. A. J. C. C. Yingst, 1965, 480-481.

53. Y. Li, *Organic optoelectronic materials*, Springer, 2015.
54. S. Garreau, G. Louarn, J. Buisson, G. Froyer and S. J. M. Lefrant, 1999, **32**, 6807-6812.
55. W. W. Chiu, J. Travaš-Sejdić, R. P. Cooney, G. A. J. J. o. R. S. A. I. J. f. O. W. i. a. A. o. R. S. Bowmaker, Including Higher Order Processes,, a. Brillouin and R. Scattering, 2006, **37**, 1354-1361.
56. W. W. Chiu, J. Travas-Sejdic, R. P. Cooney and G. A. Bowmaker, *Synthetic Met*, 2005, **155**, 80-88.
57. J. Ouyang, *Displays*, 2013, **34**, 423-436.
58. Z. Y. Zhu, C. C. Liu, F. X. Jiang, J. K. Xu and E. D. Liu, *Synthetic Met*, 2017, **225**, 31-40.
59. Y. J. Lin, W. S. Ni and J. Y. Lee, *J Appl Phys*, 2015, **118**.
60. J. P. Thomas, L. Y. Zhao, D. McGillivray and K. T. Leung, *J Mater Chem A*, 2014, **2**, 2383-2389.
61. O. Bubnova, Z. U. Khan, H. Wang, S. Braun, D. R. Evans, M. Fabretto, P. Hojati-Talemi, D. Dagnelund, J. B. Arlin, Y. H. Geerts, S. Desbief, D. W. Breiby, J. W. Andreasen, R. Lazzaroni, W. M. M. Chen, I. Zozoulenko, M. Fahlman, P. J. Murphy, M. Berggren and X. Crispin, *Nat Mater*, 2014, **13**, 190-194.
62. A. Pasha, S. Khasim, O. A. Al-Hartomy, M. Lakshmi and K. G. Manjunatha, *Rsc Adv*, 2018, **8**, 18074-18083.
63. L. V. Kayser and D. J. Lipomi, *Adv Mater*, 2019, **31**.
64. J. Rivnay, S. Inal, B. A. Collins, M. Sessolo, E. Stavrinidou, X. Strakosas, C. Tassone, D. M. Delongchamp and G. G. Malliaras, *Nat Commun*, 2016, **7**.
65. Y. Honma, K. Itoh, H. Masunaga, A. Fujiwara, T. Nishizaki, S. Iguchi and T. Sasaki, *Adv Electron Mater*, 2018, **4**.
66. D. A. Mengistie, P. C. Wang and C. W. Chu, *J Mater Chem A*, 2013, **1**, 9907-9915.
67. D. A. Mengistie, M. A. Ibrahem, P. C. Wang and C. W. Chu, *Acs Appl Mater Inter*, 2014, **6**, 2292-2299.
68. J. S. Huang, P. F. Miller, J. S. Wilson, A. J. de Mello, J. C. de Mello and D. D. C. Bradley, *Adv Funct Mater*, 2005, **15**, 290-296.